PSI Proposal No. R-21-02.1
Status report 2024 of the search for the muon electric dipole moment

M. Giovannozzi
CERN: Beams Department, Esplanade des Particules 1, 1211 Meyrin, Switzerland

M. Hoferichter
UB: University of Bern, Bern, Switzerland

G. Hiller
UD: University of Dortmund, Dortmund, Germany

R. Appleby, I. Bailey, A. Bainbridge
CI: *Cockcroft Institute, Daresbury, United Kingdom*

C. Chavez Barajas, T. Bowcock, J. Price, N. Rompotis, T. Teubner, D. Vasilkova, G. Venanzoni, J. Vossebeld
UL: University of Liverpool, Liverpool, United Kingdom

R Chislett, G. Hesketh
UCL: University College London, London, United Kingdom

N. Berger,A. Kozlinsky, F. Wauters
UMK: University of Mainz - Kernphysik, Mainz, Germany

A. Keshavarzi, M. Lancaster
UM: University of Manchester, Manchester, United Kingdom

F. Trillaud
UNAM: Universidad Nacional Autonma de Mexico, Mexico City, Mexico

B. Märkisch
TUM: Technical University of Munich, Munich, Germany

A. Baldini, L. Bianco[1], F. Cei, M. Chiappini, M. Francesconi, L. Galli, G. Gallucci, M. Grassi, F. Leonetti[1], A. Papa[2,3], M. E. Tegano[1], A. Venturini[1]
INFN-P: INFN and University of Pisa, Pisa, Italy

G. Cavoto, S. Mariottini[1], D. Pasciuto, F. Renga, C. Voena,
INFN-R: INFN and University of Roma, Roma, Italy

S.Y. Hoh, T. Hu[1], K.S. Khaw, J.K. Ng[1], Y. Shang[1], Y. Takeuchi, G.M. Wong[1], Y. Zeng[1]
SJTU: Shanghai Jiao Tong University and Tsung-Dao Lee Institute, Shanghai, China

A. Adelmann, C. Calzolaio, R. Chakraborty, M. Daum, C. Dutsov, W. Erdmann, D. Höhl[3,4], T. Hume[3,4], M. Hildebrandt, A. Jäger[3,4], P. Juknevicius[3,4], H. C. Kästli, L. Morvaj, D. Reggiani, D. Sanz-Beccera, P. Schmidt-Wellenburg[1]
PSI: Paul Scherrer Institut, Villigen, Switzerland

K. Kirch[2]
ETHZ: ETH Zürich, Switzerland

L. Caminada[2], A. Crivellin
UZ: University of Zürich, Zürich, Switzerland

February 3, 2025

---

[1] Master or PhD student
[2] Spokesperson
[3] also at PSI
[4] also at ETHZ

Contents

I. SUMMARY

In 2024 the muEDM collaboration investigated in three separate beam times different aspects of the muon EDM search at PSI.

muE1 Using a scintillating fiber monitor in vacuum and a calorimeter we investigated the phase space of the muE1 beam line in the "Z"-configuration, a possible configuration on which a future Phase II muEDM instrument could be mounted. We took data from momenta settings of $100\,\mathrm{MeV}/c$ and $125\,\mathrm{MeV}/c$ from backward decaying pions and $140\,\mathrm{MeV}/c$ from forward decays.

piM1 For the first time we operated a magnetic kicker within the superconducting solenoid next to two prototype detectors. This test sheds light on the magnetic pulse-induced noise in the detector electronics and investigates possible systematic effects of a persistent current oscillation during the planned muon storage. For this test, we stopped the pion in a central target and observed the positrons emitted from the muon decay.

piE1 On piE1 we mounted the PSC solenoid on a new vertical translation stage to remeasure the ToF of muons under reversing injections (clockwise and counterclockwise), and tested the muon injection trigger, core to our muon-on-request magnetic kick approach.

While the preparation and execution of three beam times on three different secondary beam lines at PSI, was mostly working smoothly, several technical features were not ready for the piE1 beam time:

Muon Kicker Early in 2024 it became clear that the dedicated power supply delivering short current pulses to the kicker coil within the solenoid would not be ready by autumn 2024. After a period reconsidering all procurement options and with the agreement of the Swiss National Foundation, we have now decided to develop the kicker power supply together with the Karlsruhe Institute of Technology. We are currently preparing the research contract and sketching a time plan until June 2026. No other commercial supplier could guarantee faster development for similar costs.

Superconducting channel In 2024 we managed to characterize the magnetic screening of Bi-2223 and massive NbTi. Unfortunately, both shield fields only up to about $140\,\mathrm{mT}$. We are therefore investigating shields made of multilayer HTS Rebco tape wrapped on a metal support tube.

Cryostat During the final design review of the cryostat required for the superconducting magnetic shield for injection, we discovered that the design intersects the existing geometry of the SC solenoid. A new engineer from PSI engineering department took over the task and the design was finished only in October 2024. Currently all parts are in production and we expect to mount the cryostat to the PSC solenoid in March 2025 for the first time.

For 2025 we are requesting a beam time of four weeks on piE1, details are described in Sec. VI A We will demonstrate the spiral injection through two superconducting shields, measure the initial spin phase of muons reaching the central region of the solenoid, and eventually demonstrate the storage of muons within the weakly-focusing field of the experiment by measuing the decay positrons with the positron tracker described in Sec. II L.

II. STATUS

A. Update on numerical simulation

1. Simulation Overview

The simulation for the muEDM experiment is split into three main parts; *fields, beamline*, and *muon decay*. All of the code for the simulations is maintained and shared using GIT, and is available to local and remote users with a muEDM account.

The electric and magnetic fields are simulated using OPERA and ANSYS, and ported into the GEANT4 based simulation. The temporal variations of these fields can also be estimated, and accounted for in the muon decay simulation. This is particularly useful for the pulsed electric fields used for muon storage.

Separate to that is the simulation of the muon decay, starting with injection, and ending with the muons or the relevant decay products leaving the active area of the experiment (or another pre-determined exit status). Using GEANT4 and G4BEAMLINE, the geometry, material composition, and placement of the detectors, storage instrumentation, and support structures are modeled. The path of the particles through these materials is simulated, taking into account multiple scattering. As well recording the truth information of the incident particles, the response of the detectors is simulated, so that, for example, the efficiency and resolution of the detectors is taken into account. After tuning, the resulting information mimics that of real data, and the same reconstruction algorithms can be run on both data and simulation. To run the simulation, users supply a *.mac* file, which can be configured to alter the geometry/performance of the detectors for systematic studies, or to start with a different set of input muons. An example of the tuning of detector response is given in section II A 3.

Often large statistics are needed for systematic studies, particularly for the more subtle effects. As such, it is important to be able to generate higher statistics for a previously run study, using identical conditions. The code is regularly updated, and it is not always possible or desirable for complete backwards compatibility. Fortunately the git framework keeps a record of the code at each point in time, so it is always possible to roll back to an earlier version to generate more statistics. In order to facilitate this, a record of the *git hash* (i.e. a unique number referring to the git version) is kept in the meta-data of every official simulation. The description of the meta-data is described in section II A 2.

2. The muEDM simulation: meta data and (re)running simulations
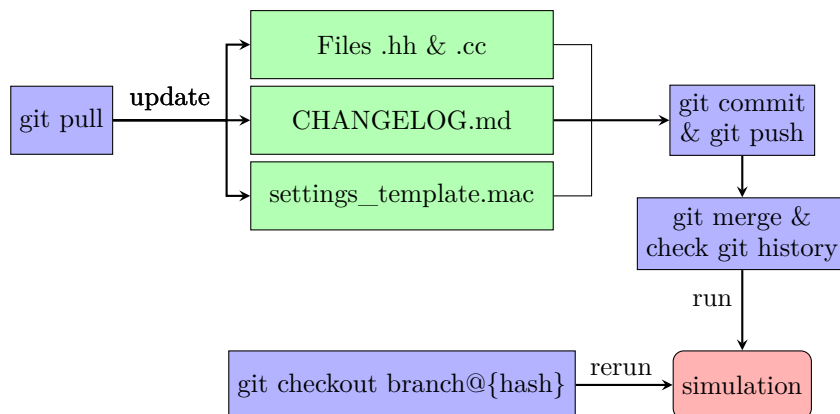

Figure 1: The flow chart shows the suggested process to update and rerun the simulation.

When running a simulation, the output is saved to a ROOT file "DetectorOutput.root" under "data_output/base_folder/job_id" together with a metafile "MetaData.txt". The metafile contains information on the simulation performed. This includes the used macro file name and its content, as well as the content of the "Parameters.hh" file. The latter describes parameters used in the simulation, while the first can change certain parameters upon running it. In addition to the code version and the time when the simulation was run, it also has the git branch and git hash. This together with the macro file can be used to rerun a previous simulation. For this, it is important to commit and push changes before running a simulation. A rough scheme of what to remember is shown in Figure 1. Upon making changes to the Geant4 model, these changes, additions, and fixes should be documented in "CHANGELOG.md" as well as the template macro file "settings_template.mac" when changing or adding commands.

*3. First MC simulations with tuned fiber behavior using data*

In order to reproduce in the MC simulation the behaviour of the CHeT fibers as measured in the laboratory, a dedicated study of the single CHeT fiber has been conducted, including dedicated measurements in the laboratory and fine-tuned MC simulations in Geant4. We will be using the SCSF-78 fiber by Kuraray, featuring a polystyrene core and a single cladding made of PMMA, with a squared section of side length $500\,\mu m$ connected to SiPMs (also MPPCs) from Hamamatsu, model S13360-1350PE. A positron beam with a monochromatic momentum of p = $2\,MeV/c$ is generated, impinging on the fiber, readout with a SiPM at each end. These events replicate the positrons corresponding to the selected energy spectrum endpoint of a ^{90}Sr radioactive source used in the laboratory. The simulation results are then compared with experimental measurements, which involve a single fiber connected to SiPMs at both ends and irradiated with a ^{90}Sr source. As an example, Fig. 2a) shows the measured SiPM spectrum for three different distances at which the positrons hit the fiber. While Figs 2b,c) show the spectra for a fixed distance of $98\,cm$, using an "OR" and an "AND" logic.
At short distances we observed a rapid reduction in rates with increasing distance, see Fig. 2a). To analyze this effect, the simulation was repeated with different combinations of values for refractive index of core and cladding, shown in Fig. 3. The effect is only present when the values differ. For larger distances we found an exponential decay with a characteristic length smaller than initially set in the MC. It was adjusted to match the experimental data, $4\,m$, also in accordance with the value from the datasheet.

In the simulation a sensitive volume with a squared section of $1.3\,mm$ width was added to each end of the fiber. A broadening of the spatial distribution of events in the sensors was observed when increasing the thickness of the optical paste. We fixed the value to $400\,\mu m$.
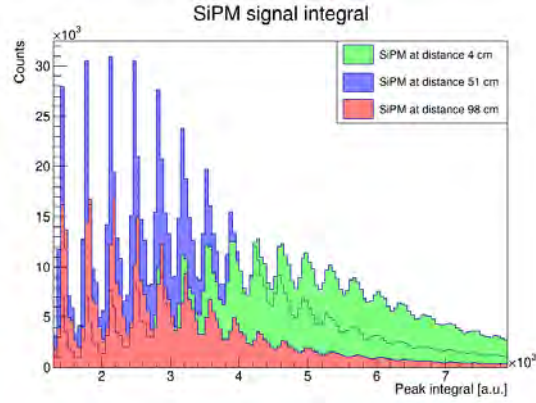
(a)
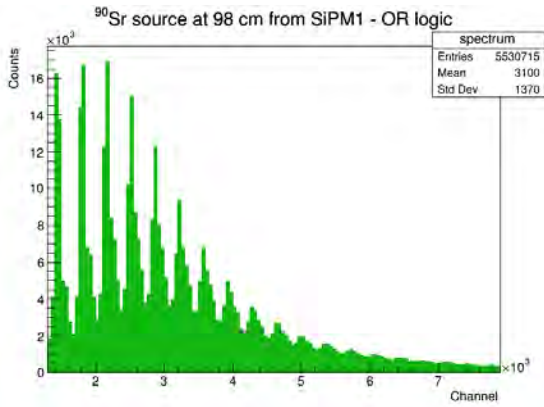
(b)
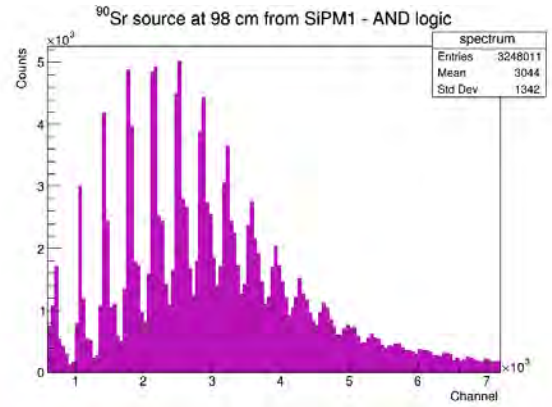
(c)

Figure 2: Output spectrum of the SiPM signal with a fiber 100 cm long and a ^{90}Sr source at different distances, and for a distance of 98 cm in OR and AND trigger logic of the SiPM at the two ends.
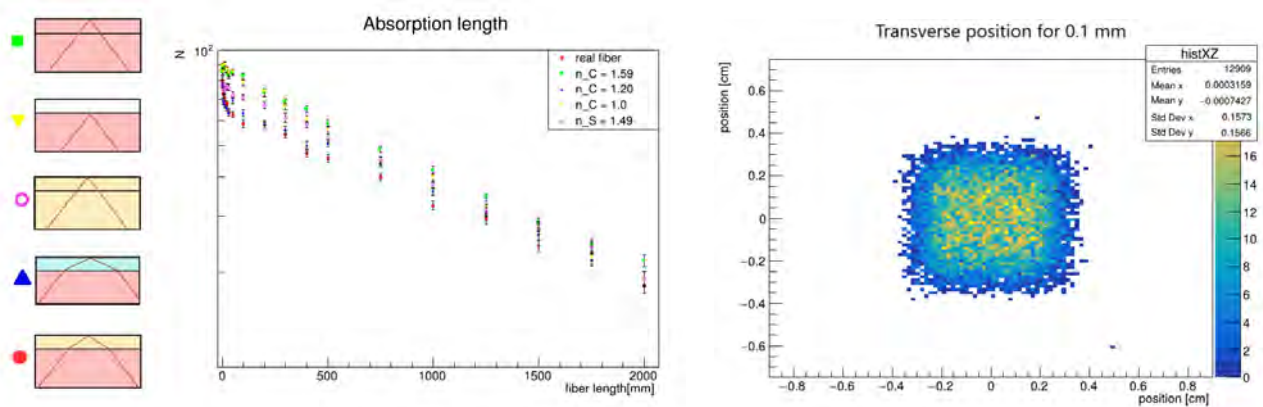
(a)
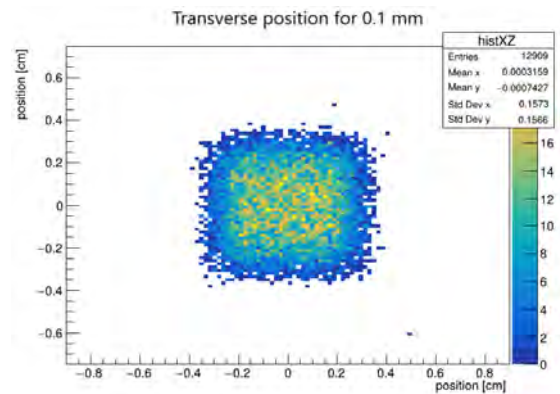
(b)

Figure 3: (a) Number of photons at the sensor vs distance between the positron beam position and the sensor, for different refractive index of cladding and core (in the sketch, each color is a different value of refractive index. (b) Transverse position of photons at the sensor, for an optical cement width of $100\,\mu m$.
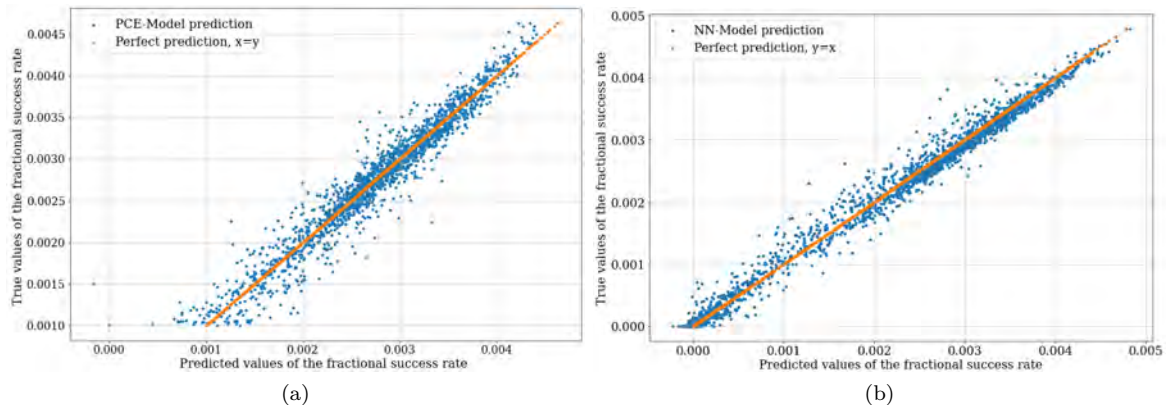
Figure 4: Comparison between true (orange) and predicted injection efficiency (blue) for PCE based surrogate model (a) and NN based surrogate model (b).

4. Beam injection optimization using a surrogate model

In the latest efforts towards fast design optimization of the precursor experiment, an MOEA (Multi-Objective Evolutionary Algorithm) called NSGA-II (Non-dominated Sorting Genetic Algorithm) [1] has been implemented which has been very successful in various multi-objective optimization problems in recent times [2]. Within NSGA-II the objective evaluation is done using a surrogate model to accelerate computation. In the next two subsections, two optimization campaigns, with $28\,\mathrm{MeV}/c$ and $22\,\mathrm{MeV}/c$ muons, are described briefly. The current in the weakly focusing coil is fixed at $1.5\,\mathrm{A/mm}^2$ and the shape of the time-dependent magnetic kick is imported from another simulation using a circuit design tool[5]. Both campaigns were carried out using a distribution of 3×10^6 muons at the end of collimation tubes to restrict the uncertainty of successful muon storage to below 1 %.

To simultaneously maximize the injection efficiency and minimize the heat dissipated by the large correction coil for $28\,\mathrm{MeV}/c$ muons, two surrogate models, one constructed using PCE and the other using NN are trained on an input distribution over design parameter ranges as given in Table I. The distribution is based on Sobol sequences [3] and is generated using the Python software toolbox Chaospy [4]. Within this toolbox, a d-dimensional joint distribution of n points can be generated using *rule='Sobol'* in Chaospy sampling. For training surrogate models n = 12000 configuration points were run using G4Beamline[6] [5].

Table I: Design variable range of input distribution

Physics Parameter	Symbol	Lower Bound	Upper Bound
Kicker Pulse Time Offset [ns]	T_offset	80	98
Kicker Pulse Strength [arb. unit]	BPI	0.35	0.80
Correction Coil Length [mm]	CC_len	88	150
Correction Coil Inner Radius [mm]	CC_ir	40	84
Correction Coil Thickness [mm]	CC_thick	7	15
Correction Coil Position [mm]	CC_pos	166	241

To train a PCE surrogate model, the configuration points corresponding to a fractional storage efficiency below 0.001 are discarded as it is found that the model performance is skewed otherwise. As a result, out of 12000 points, 4620 points are used for training and 1850 points are used to test the performance of the model. Polynomial order 6 results in the least mean squared error (3.48×10^{-8}) between the prediction of the model and the simulation result. On the other hand, the NN surrogate model is built based on a previous study of hyperparameters [6]. The model is implemented in PYTORCH [7] and is trained on a network of 8 hidden layers with 500 neurons in each layer. The NN model is optimised using Adam optimizer [8], uses leaky RELU [9] as activation function, has ReduceLROnPlateau [10] as a learning rate

---

[5] https://www.analog.com/en/design-center/design-tools-and-calculators/ltspice-simulator.html
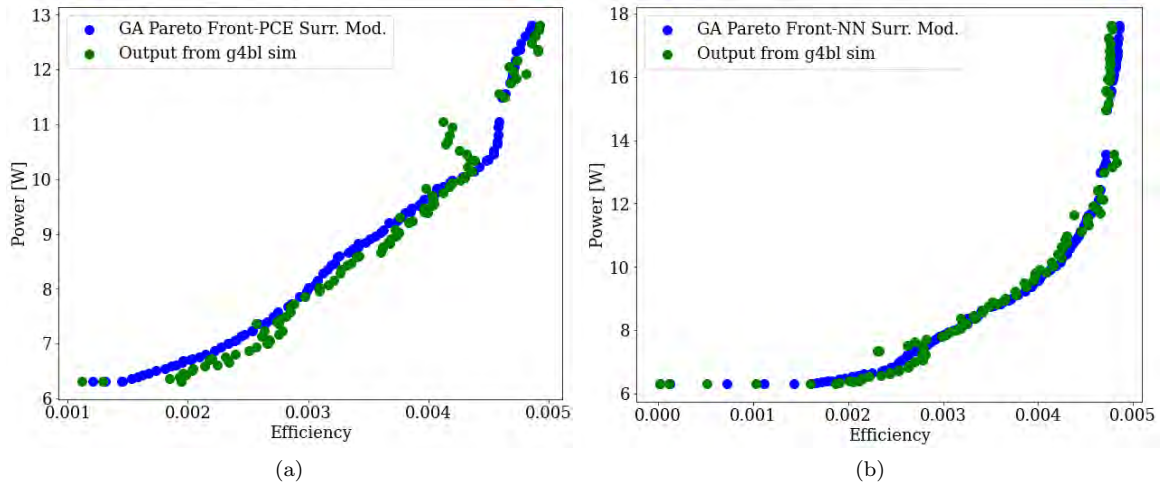[6] https://www.muonsinc.com/Website1/G4beamline

Figure 5: Comparison between GA optimised pareto front obtained from (PCE (a) and NN (b)) surrogate model (blue) and simulation output (green).

scheduler, and does not include any regularisation. The model is trained using 9000 points and the rest 3000 points are used to benchmark the performance of the model. The mean squared error between the prediction of the model and the simulation result in this case is 1.89×10^{-8} A comparison of the surrogate model performance for PCE and NN based models is shown in Fig. 4.

The use of surrogate models in the GA to find the optima instead of the G4Beamline simulations results in orders of magnitude speed-up in the optimization campaign. In this case, the MOEA that simultaneously maximizes muon storage efficiency and minimizes power dissipation in correction coils can be run ~10^3 times faster using a PCE-based surrogate model and ~10^4 times faster for a NN-based surrogate model. The comparison between the pareto optimal solutions obtained from GA based on surrogate models and the simulation output for these solutions is shown in Fig. 5. The agreement is within 5% for the PCE surrogate model and within 2% for the NN surrogate model for an average storage efficiency of 0.35%.

5. Beam injection and storage studies based on Bayesian optimization

PCE is suited for uncertainty quantification and optimization but becomes computationally demanding with higher dimensionality, requiring many training points. It is also less robust to data noise, limiting its effectiveness. To address these challenges, we chose Bayesian Optimization (BO), which efficiently optimizes costly black-box functions without explicit derivatives. Using a probabilistic surrogate model, typically Gaussian Process (GP) regression, BO balances exploration and exploitation, minimizing evaluations needed to find the global optimum. This makes BO ideal for noisy, resource-constrained, and computationally expensive situations, including simulation-based design task configurations.

For implementing the BO algorithm, a GP serves as the surrogate model. The GP offers a probabilistic framework for modeling the objective function $f(x)$, which is assumed to follow a distribution represented by:

$$f(x) \sim \mathcal{GP}(\mu(x), k(x, x')) \tag{1}$$

where $\mu(x)$ denotes the mean function, encoding prior beliefs about the function's behavior, and $k(x, x')$ is the covariance function or kernel, which captures the similarity between points x and x'. The kernel function $k(x_i, x_j)$ utilized in the GP model is defined as:

$$k(x_i, x_j) = \sigma^2 k_{RBF}(x_i, x_j) + \sigma_{\text{noise}}^2 \delta_{ij} \tag{2}$$

where $k_{\text{RBF}}(x_i, x_j)$ is the Radial Basis Function (RBF) kernel, commonly used for its smoothness properties, and σ_{noise}^2 is a noise term that accounts for uncertainty in the observations. The term δ_{ij} ensures that the noise is added only to the diagonal elements, reflecting the independent observation noise. The RBF kernel, often known as the squared exponential kernel, is defined as:

$$k_{RBF}(x_i, x_j') = \sigma_f^2 \exp\left[-\frac{1}{2} \sum_{d=1}^{D} \left(\frac{x_{i,d} - x_{j,d}'}{l_d} \right)^2 \right] \tag{3}$$

where σ_f^2 is the variance of the function, l_i is the length scale for each dimension, and D is the dimensionality of the input

space. This kernel guarantees a smooth interpolation of the objective function and incorporates the effects of scale and variability in the data. The surrogate model approximates the objective function, which, in this scenario, is derived from computationally expensive simulations utilizing the G4Beamline framework. To determine the next evaluation point, an acquisition function, specifically the Upper Confidence Bound (UCB), is employed. The UCB is defined as:

$$\alpha(x) = \mu(x) + \kappa\sigma(x) \tag{4}$$

where κ is a hyperparameter that balances exploration (sampling areas of high uncertainty) and exploitation (sampling areas with high predicted mean values). The next evaluation point is chosen by maximizing the acquisition function:

$$x_n = \text{argmax}_x\alpha(x|D_{t-1}) \tag{5}$$

where D_{t-1} represents the data collected up to the prior iteration. This approach guarantees an efficient search for the global optimum by iteratively refining the surrogate model and directing evaluations to the most promising areas.

To prototype the BO, a set of starting points is required, representing the injection parameters of interest. These parameters are initially scanned within their respective initial ranges, with the chosen ranges defined to cover 60

Parameter symbol	Physics parameter	Lower bound	Upper bound
Theta	Injection angle (degree)	-45	-42.2
Phi	Transverse angle (degree)	10	24
InjR	Injection radius (mm)	32.2	47
Z	Longitudinal injection coordinate (mm)	-450	-439
WeakCurr	Weak coil current (x 100 A)	68	380
BPI	Kicker field strength (a.u.)	0.6	2.4
ptoffset	Time offset of pulse kicker (ns)	-28	16

Table II: List of parameters and initial ranges.

Next, a low-discrepancy sequence generator known as the Sobol sequence is used to create 10 uniformly distributed sample points within the specified ranges for each parameter. These sample points serve as an initial input for the BO process. The hyperparameters of the Gaussian Process kernel are established by fitting Eq. 2 to the scanned initial parameter ranges through the maximum log-likelihood estimation method. The hyperparameters obtained are summarized in Tab. III.

Parameter symbol	Physics parameter	σ^2_{noise}	σ^2_f	l_d
Theta	Injection angle (degree)	1.28×10^{-4}	0.123^2	2.36
Phi	Transverse angle (degree)	1.79×10^{-4}	0.155^2	12.1
InjR	Injection radius (mm)	2.6×10^{-4}	0.177^2	11.3
Z	Longitudinal injection coordinate (mm)	5.41×10^{-5}	0.126^2	8.22
WeakCurr	Weak coil current (x 100 A)	6.89×10^{-6}	0.156^2	50.2
BPI	Kicker field strength (a.u.)	4.12×10^{-5}	0.127^2	0.381
KPT	Time offset of pulse kicker (ns)	2.3×10^{-5}	0.112^2	6.58

Table III: List of hyperparameter extracted from the fit.

For each set of injection parameter inputs, the stored muon efficiency ϵ is defined as:

$$\epsilon = \frac{N_{stored}}{N_{injected}} \tag{6}$$

where N_{stored} represents the number of muons that meet the following criteria:

Disable the muon decay process, position a virtual plane at the center of the solenoid ($|z| < 40mm$), and count the event IDs of muons that remain for more than 300 ns in the virtual plane. Furthermore, $N_{injected}$ represents the total number of injected events.

The BO process used 100,000 events sampled from the injection phase-space distribution, running for 50 iterations over roughly 150 hours. Each iteration predicts the next optimal point, which is added to the initial 10 input points. The performance of the single-objective BO, guided by the Upper Confidence Bound (UCB) acquisition function, is illustrated in Fig. 6.

The optimized set of injection parameters (Yu-V1), which corresponds to the highest efficiency achieved, is derived from Fig. 6. This result shows significant improvements compared to the previous set (Rit-V1), where the stored muon efficiency is 0.324
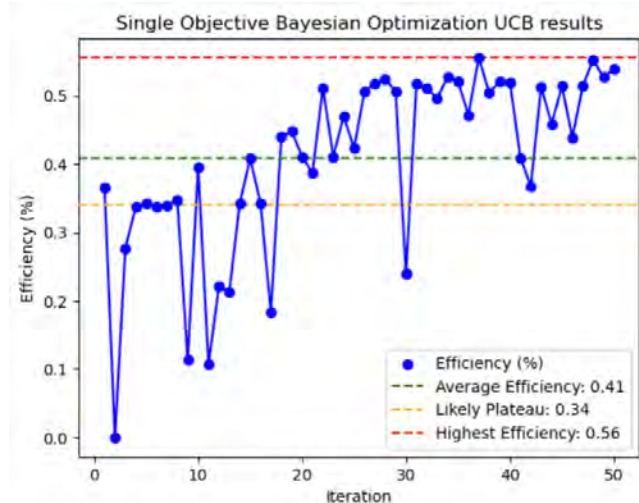
Figure 6: The muon storage efficiency for each iteration.

The detailed comparison of the optimized injection parameters between the PCE method (Rit-V1) and Bayesian Optimization (BO) (Yu-V1) is summarized below Tab. IV. However, this improvement comes with specific trade-offs:

Parameter symbol	Physics parameter	Rit-V1	Yu-V1
Theta	Injection angle (degree)	-45.022	-45
Phi	Transverse angle (degree)	9.244	17.464
InjR	Injection radius (mm)	45.561	43.160
Z	Longitudinal injection coordinate (mm)	-443.836	-450
WeakCurr	Weakly focusing coil current (x 100 A)	150.0	202.899
BPI	Kicker field strength (a.u.)	1.0	1.497
ptoffset	Time offset of pulse kicker (ns)	0	-28
ϵ	Stored muon efficiency (%)	0.324	0.556

Table IV: The optimal parameters from PCE (Rit-V1), and from BO (Yu-V1), this work.

1. Higher weakly focusing coil current (WeakCurr): Increased from 1.5 to 2.029, requiring a higher power input to maintain coil operation.

2. Higher kicker field strength (BPI): Increased from 1.0 to 1.497, indicating a stronger magnetic field kick to guide the muons into the storage region.

3. Earlier pulse kicker time offset (ptoffset): Adjusted from 0 ns to -28 ns, to delay the kicker activation time during the beam injection process.

These adjustments collectively optimize the injection phase space to achieve higher storage efficiency, albeit at the expense of more demanding operational requirements parameters.

B. Magnetic optimization of superconducting solenoid for Phase II

Phase II will be using backwards decaying muons with a momentum of $p \leq 215 \, \mathrm{MeV}/c$. For an optimal matching of the injection phase space to the acceptance phase space we are optimizing the magnetic design of a dedicated superconducting solenoid to trap muons. For this, we have set up a finite element model of a superconducting solenoid. The specifications are 3±0.003 T at a radius of 140 mm off the central axis of the solenoid with a difference between the central magnetic field at $z = 0$ and the field at ±500 mm of the center of -1‰(see Fig. 7). The field magnitude must increase monotonically from the point of injection to the center of the solenoid. The model is constructed in the software Gmsh [11] and the magnetic field is solved with the finite element solver GetDP [12].

Here, the system is assumed to be axis-symmetric and the effects of injection are excluded. Figure 8 shows the mesh, where each block represents a potential sub-division of the solenoid. A specific current density is assigned to each block. The target magnetic field is given in Fig. 9. In this first approach, the objective is a monotonic B_z field (new target), the desired B_r and B_z fields, including the weakly-focusing field in the center are shown alongside. The problem is
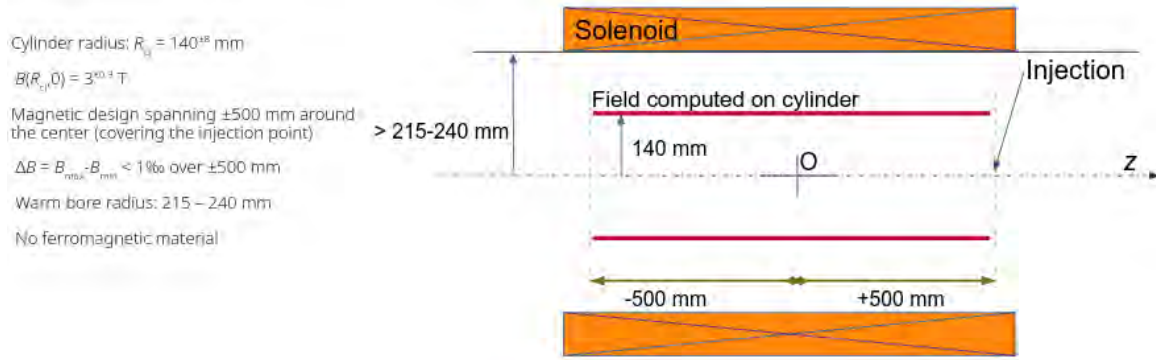
Figure 7: Schematic drawing and specifications for the magnetic field at 140 mm off axis.
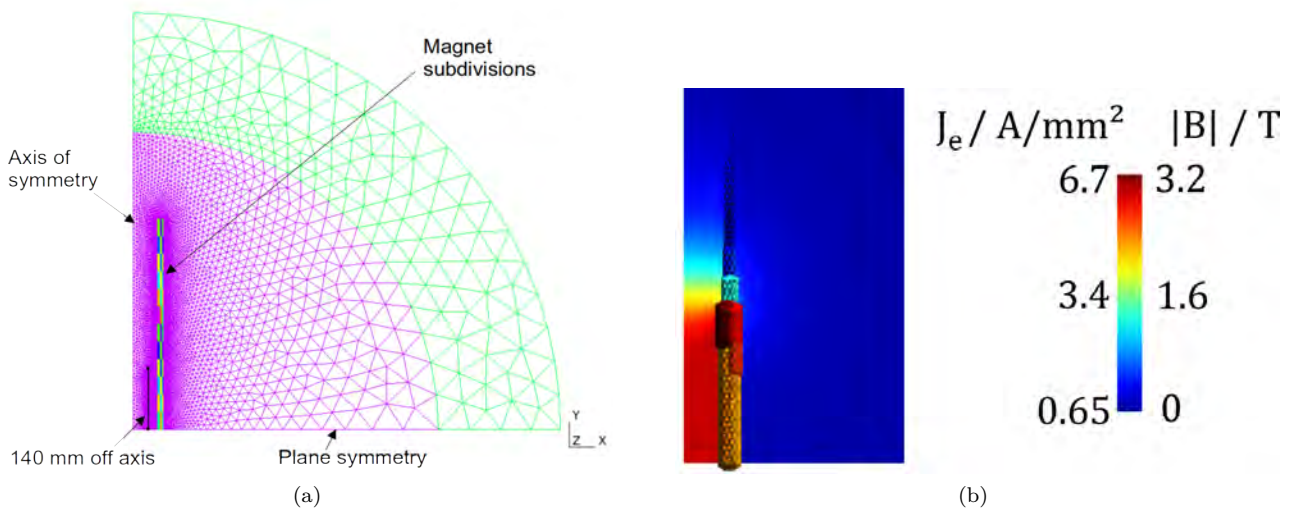

(a)

(b)

Figure 8: (a) Mesh of the finite element model to optimize the configuration of the superconducting solenoid. The solenoid is divided into 36 subdivisions (3x12). (b) Result of FEM simulation: current densities and magnetic field over the model.

formulated as an inverse problem, aiming to determine the appropriate set of current densities required to generate the specified B_z field in the target region (from -500 mm to 500 mm around the magnetic center). Hence, the B_z field produced by each individual block shown in Fig. 8 is represented in a single matrix, leading to the following system of equations:

$$B_c J = B_t, \tag{7}$$

where B_c is a matrix where each column j corresponds to the $B_{z,j}$ field along the axis at a distance of 140 mm from the center line, produced by a current density J_j in block j. The columns are then the value of the field at a given position along the axis. The vector J indicates the different current densities J_j and B_t is the specified B_z along the axis. Figure 9a shows the preliminary results using singular value decomposition and regularization to compute the pseudo inverse B_c^+ to find a solution J_s to (7) ($J_s = B_c^+ B_t$).

C. Technical design overview

Phase I of the MuEDM Experiment comprises six key components: the storage magnet, injection, trigger system, field manipulation, magnetic kick, and tracking system. This section provides an overview of the technical design of each component and describes its current status and role in the overall setup. The sections that follow detail the characteristics and current status of each component.
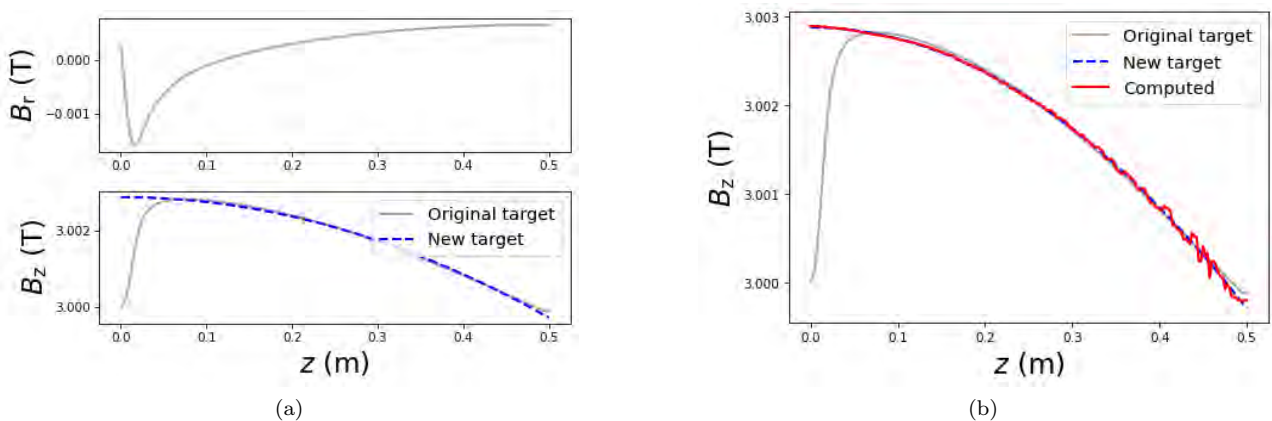
(a)   (b)

Figure 9: (a) Objective field: top figure showing the B_r field along the z axis of the solenoid and bottom figure showing the B_z field at 140 mm off axis. A new target for the B_z field is considered as shown by the blue dashed. (b) Comparison of target field and computed B_z field. Note that the weakly-focusing field in the center will be generated by a dedicated coil close to the storage orbit.

1. Solenoid Magnet

To store muons with a momentum of 22 MeV in an orbit of 30 mm radius, a magnetic field of 2.45 T is required. In Phase I of the muEDM experiment, we use an existing superconducting solenoid (see Figure 10) capable of generating fields up to 5 T. This magnet has a 200 mm-diameter bore and a length of 1 m, providing space for the detectors, the electrodes required by the frozen-spin technique, and coils for the weakly-focusing field and field trimming.
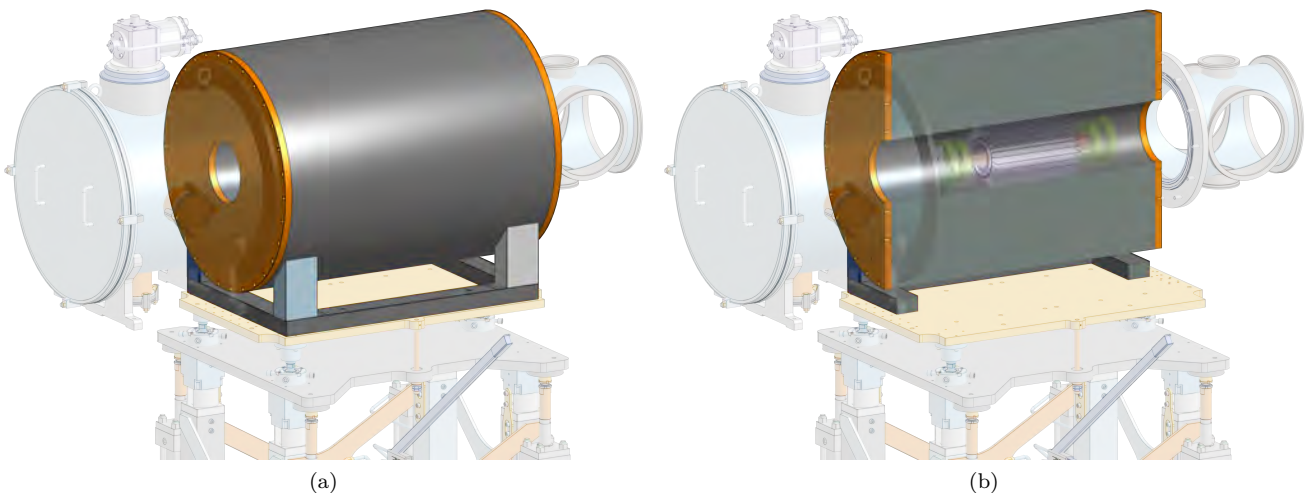

(a)   (b)

Figure 10: A CAD rendering of muEDM experiment. (a) Externa and (c) cross section view of the SC solenoid.

2. Injection

The injection system introduces muons into the PSC magnet off-axis at an position close to one end of the bore, allowing them to spiral into the center and finally orbit at a 30 mm radius in either clockwise (CW) or counterclockwise (CCW) direction. To mitigate the effects of the magnet's stray field on the incoming beam, passive magnetic shielding is used.

a. Experiment Lifter

Because muons enter off-axis, the experiment must be lowered by 46.3 mm from the central position for CW injection or
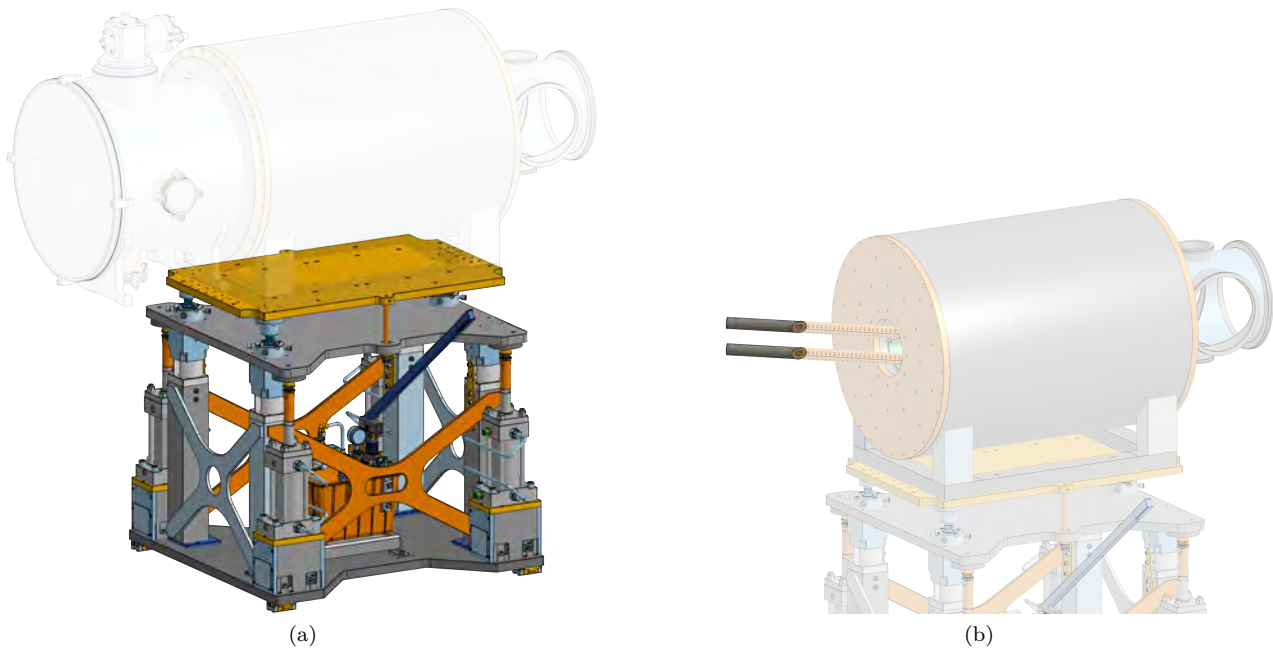
Figure 11: (a) CAD rendered image of the experiment lifter. (b) CAD rendering of the experiment, highlighting the magnetic steel tubes.

raised by the same amount for CCW injection. To achieve this vertical adjustment, the experiment lifter was designed and constructed (see Figure 11a). It supports loads exceeding 1.6 t, surpassing the total anticipated mass of the experimental apparatus. The vertical translation is powered by four manual oil translation stages activated by a manual pump. The vertical positions are established by four precisely machined stoppers inserted into the translation stages and blocked. Its performance was successfully demonstrated during a test beam in October 2024.

b. Low Magnetic Field Passive Shielding

Magnetic steel tubes, each with an inner diameter of 15.3 mm, an outer diameter of 40 mm, and a minimum length of 250 mm, are positioned around the beam path (see Figure 11b). These tubes shield stray magnetic fields of up to about 100 mT. Their small inner diameter also acts as a collimator, filtering out muons with an unfavorable phase space for storage.

c. Vacuum Chamber

Preserving the phase space and momentum of the muons is critical for maximizing storage efficiency and maintaining precise momentum control. Consequently, the experiment is maintained under a vacuum of approximately 1×10^{-6} mbar. Achieving such a low pressure also facilitates cooling of the materials required to shield the muons from stronger stray fields produced by the PSC magnet, as discussed below.

Vacuum pumping is performed from both ends of the PSC magnet. On the upstream side, a dedicated vacuum chamber is in production and will house a cryostat. On the downstream side, a vacuum cross was designed and will be ordered soon, to accommodate additional equipment, cables, and piping, while also providing space for feedthroughs for devices located inside the PSC magnet's bore. Figure 12 shows a CAD model of the vacuum chamber and the vacuum cross.

d. Cryostat

To shield the incoming muons from stray magnetic fields close to the bore on the order of 1 T, a magnetic screen made of superconducting material will be used. These materials must be cooled below their critical temperature, ideally to less than 5 K, so a dedicated cryostat was designed to house the tubes and interface with a cryo-cooler (Sumitomo, SRDK-408D2), featuring a two-stage cooling system capable of lowering the temperature to around 3.83 K, keeping the tubes below their respective critical temperatures.

e. Passive Shielding for High Magnetic Field

Cooled below their critical temperature, persistent currents induced in a sc magnetic shield while ramping the solenoid field shield the muons from the transverse magnetic field along the path to the injection point, located inside the PSC magnet's bore (see Fig. 14). Field simulations indicate a magnetic field of abouth 1.2 T in the injection, a fraction of that perpendicular to the muon injection paths (see Fig. 22). Shielding of the transverse field is paramount to maximize transmission of the injection. A design of these tubes is shown in Fig. 14, and additional research on their properties is
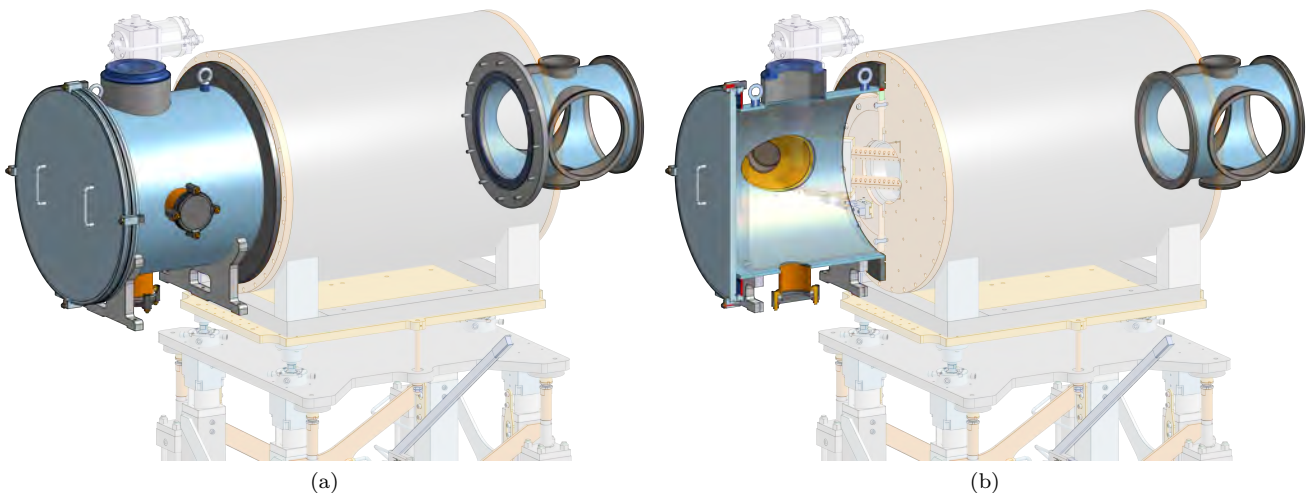
Figure 12: (a) CAD model of the vacuum chamber and vacuum cross. (b) Cross section of the vacuum vomponents.
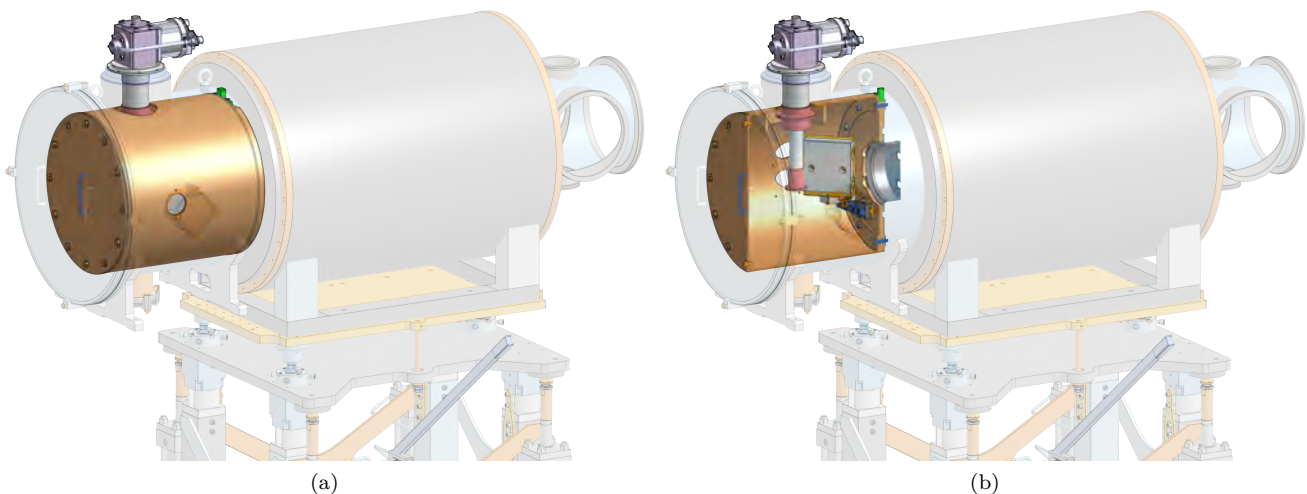

Figure 13: (a) CAD renderings of the cryostat and its internal structure. (b) Cross sectional view showing the first and second stage of the cryo-cooler and the 50 K-shield.

discussed in Sec. II F.

Ideal numerical simulations performed in Ansys with an ideal superconducting material ($\mu_r \approx 0$ and $\sigma \to \infty$S) estimate a maximum total force of about 56 kg acting on the superconducting tubes when they completely shield the transverse field component. In practice, some degree of incomplete shielding is expected, leading to smaller forces.

3. Trigger System

Once muons have passed through the passive magnetic shielding tubes into solenoid bore, a trigger signal must be generated for those muons that have the correct phase space to be stored at the center of the magnet. The magnetic kicker (described in Sec. II D 1) must be activated within 100 ns—the time it takes for suitably phased muons to travel from the entrance detector to the central region of the PSC magnet's bore.

As shown in Figure 15, the trigger detector consists of two detectors: a thin gaate scintillator and a thicker aperture scintillator with holes. A muon within the correct phase space generates a signal in the entrance scintillator and passes through the holes in the aperture scintillator, while muons not mathcing to the storage phase space also create a signal in the aperture scintillator. Taking the anti-coincidence between gate and active aperture the electronics of the trigger detector produces one LVTTL signal when a storable muon is detected. Further details of the trigger detector are
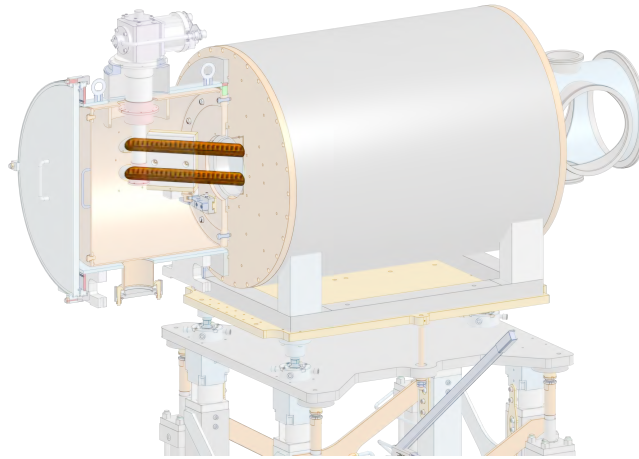
Figure 14: Image of CAD of superconducting tubes inside the cryostat.

(a)   (b)
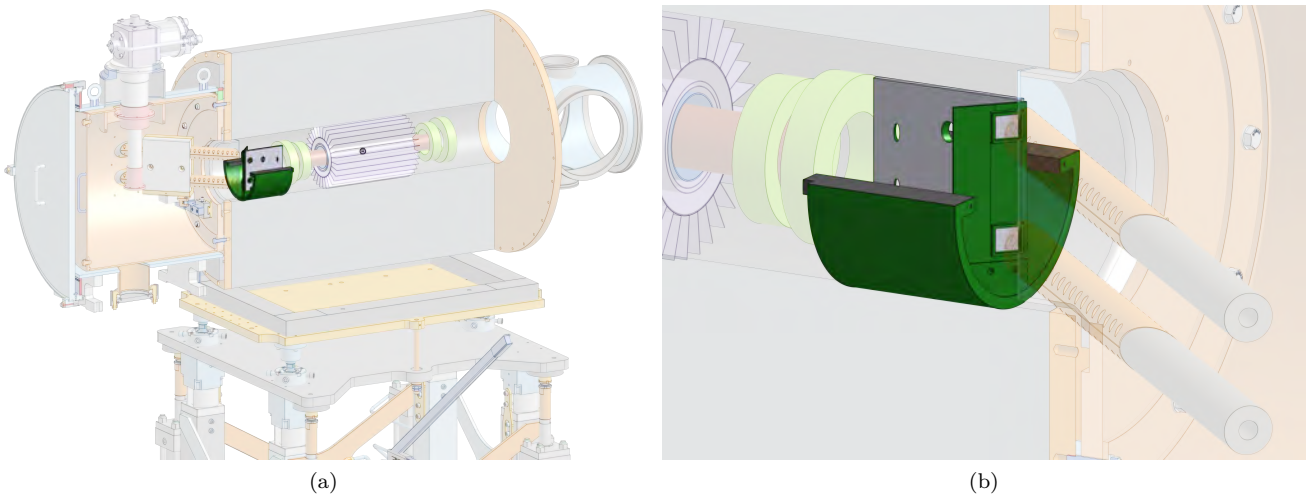
Figure 15: CAD renderings of the trigger detector. (a) Trigger detector highlighted inside the PSC magnet. (b) Lateral view of the trigger detector showing the trigger windows and the aperture scintillator.

discussed in Section II J.

D.   Magnetic Field Correction

The axial magnetic field of the PSC magnet exhibits two peaks (sometimes know as "bumps") at approximately ±225 mm from its center, which can reflect incoming muons and thus reduce storage efficiency. To correct for this, a set of correction coils was designed to make the field monotonic up to the central region, where an additional smaller coil creates a weakly-focusing field to trap muons at the center of the solenoid. Figure 16 shows a CAD model of these correction coils, and Fig. 17 compares the axial field profile before and after their addition.

1.   Magnetic Kicker

To kick the muons onto a closed orbit at 30 mm radius at the center of the solenoid, a dedicated coil produces a brief magnetic pulse. This coil resembles an anti-Helmholtz configuration, a split coil pair with reversed currents. The coil is divided into four quadrants to minimize inductance and, therefore, the required driving voltage. The current supply must deliver a short current pulse to generate a short damped pulse of 200 A lasting about 50 ns. A dedicated development of this pulse generator is subcontracted to the Karlsruhe Institute of Technolgies. For the test beam in
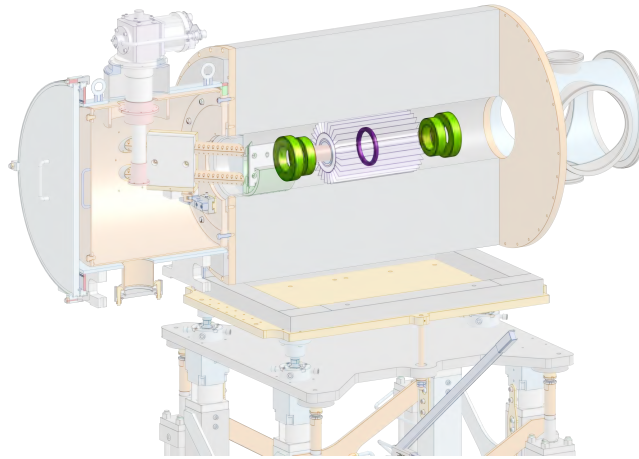
Figure 16: A CAD model of the correction coils and the weakly focusing coil to adjust the magnetic field inside the PSC magnet to optimize storage efficiency.
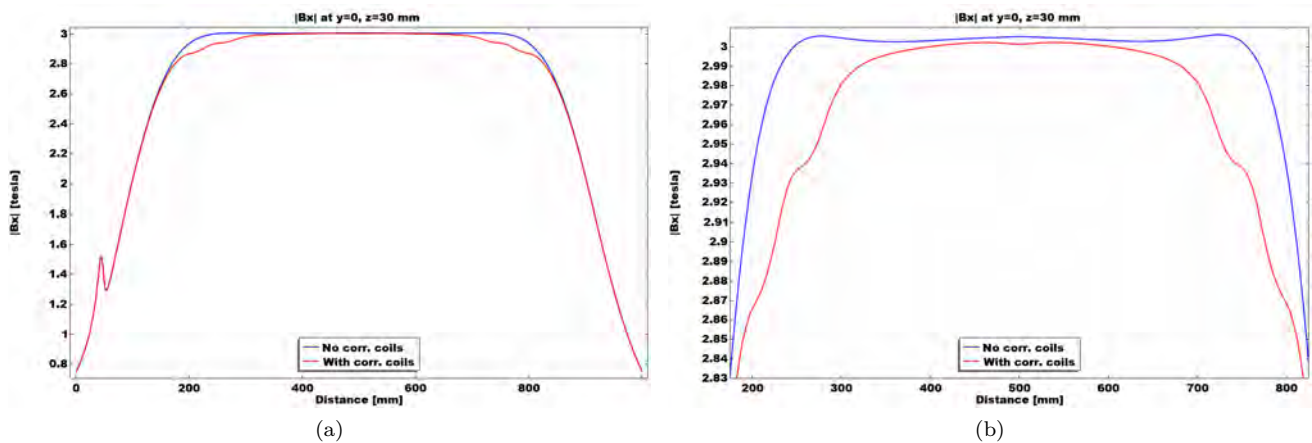

Figure 17: Comparison of the axial field without (blue) and with (red) correction coils. The muons are injected at distance= 0 mm and are stored at distance 500 mm. (a) B-field along the solenoid axis at a radius of 30 mm. (b) Closeup view of the field showing the local maximum without the correction coils, and the monotonically increasing field towards the center with correction coils.

2025 an under-damped pulse of approximately 50 A can be used for demonstration purposes. Figure 18 shows the coil's design, which is described in more detail in Sec. II G and Sec. II H.

2. Tracking System

To detect changes in the spin precession of stored muons under the frozen-spin technique, a tracking detector named $CHeT$ will measure the decay positrons. As illustrated in Fig. 19, the detector's "petals" and cylindrical body are composed of scintillating fibers. Section II L provides further details on the detector design.

E. Correction and weakly-focusing coils

The correction coils and weakly-focusing coil form a system of electromagnetic coils within the vacuum chamber, designed to shape the magnetic field generated by the main solenoid. Their primary function is to prevent muon reflection and create a small central dip in the flux density to enable muon trapping. The field must increase smoothly and monotonically toward the center, where the dip is located, any abrupt variations could lead to muon reflection. A coil structure was modeled by the Daresbury Laboratory team using OPERA, a finite element software that employs a
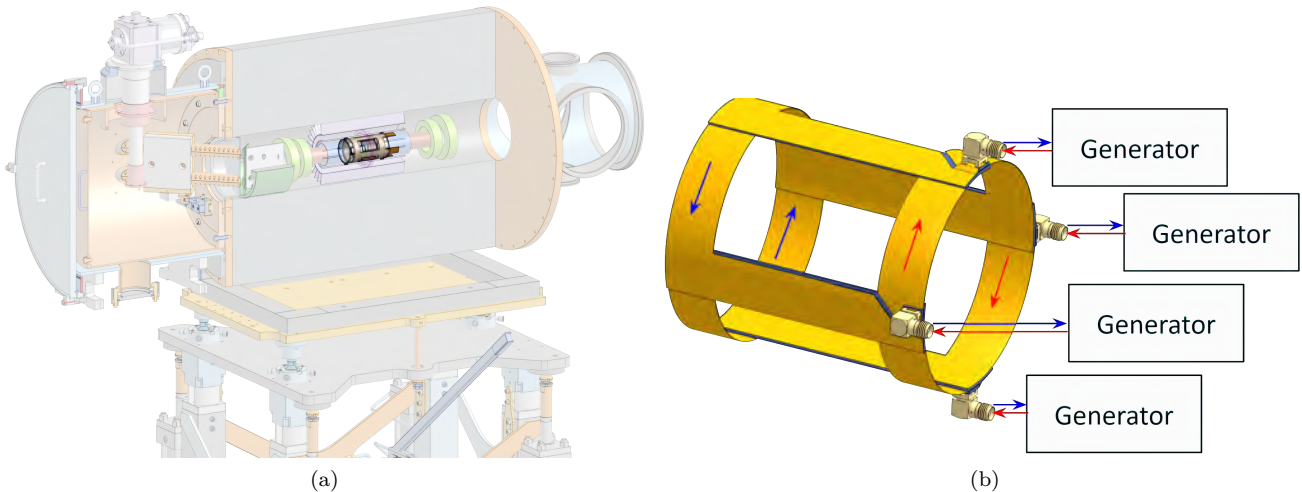
Figure 18: CAD renderings of the magnetic kicker coil. (a) Highlighed position where the kicker coil will be located inside the solenoid magnet. (b) Closeup look to the kicker coil showing its segmented structure into 4-subcoils, and the direction of the induced pulsed current.
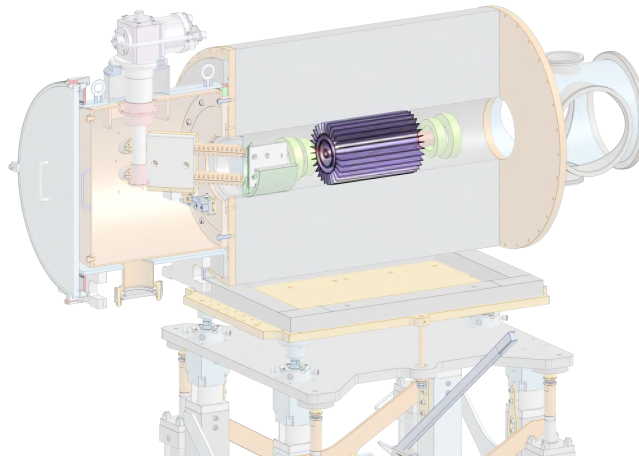

Figure 19: A CAD rendering of the CHeT tracking detector.

proprietary Biot-Savart technique, enabling highly accurate coil field simulations without the constraints of traditional meshing. The design was optimized to achieve the desired field profile (see Fig. 20), which decreases monotonically away from the central dip and provides efficient trapping of the muons.

There are five coils in the corrector coil set; a central trap coil and two coils on either side between 220 mm and 300 mm of the longitudinal center, which shape the field entrance and exit. The central trap coil extends from 50 mm to 60 mm in radius and is 10 mm long. The two inner corrector coils extend from 40 mm to 60 mm radius and are 30 mm long. The two outer correction coils extend from 40 mm to 70 mm radius and are 30 mm long. The coil positions, inner radii, and outer radii are specified to avoid mechanical clashes and to ensure compatibility with the detector components. The coils will be wound from vacuum-compatible Kapton-coated copper wire of 2 mm diameter. The inner corrector coils operate at a current density of 1.18 $A\text{mm}^{-2}$, dissipating 3 W of thermal power each, and the outer corrector coils operate at a current density of 1.57 $A\text{mm}^{-2}$, dissipating 8.5 W of thermal power each. Thermal modeling was performed which highlighted difficulties in ensuring that heat was able to flow from the central turns into a heat sink; to solve this the coils will be wound and vacuum impregnated with UHV epoxy by specialists at the Rutherford Appleton Laboratory (RAL), UK. A detailed coil mounting and cooling structure has been designed which also accommodates the detector. The expected power dissipation of the coils, in total, is 25 W which must be prevented from heating the superconducting components. Each coil will be mounted on an aluminum former, which will be water cooled by a copper pipe leading to a feed-through on one end of the chamber, which will be sufficient to remove heat from the system. Thermal modeling verified that relying on conduction along the coil mount would lead to excessive radiative heating of the cold parts of the experiment. The CAD design of the coil mounting system in its current state is shown in Fig. 21.

The current status of the coil arrangement is that the design of the coils themselves has been finalized, the wire has
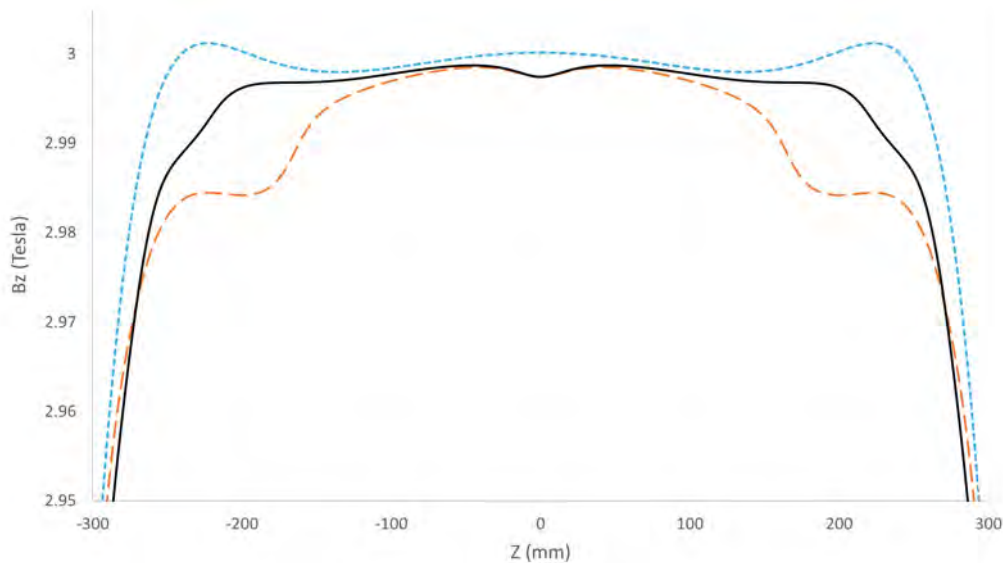
Figure 20: The simulated longitudinal component of the magnetic field in the experiment at a radius of 31.13 mm (corresponding to the muon storage radius). The blue dotted line represents the uncorrected field from the superconducting solenoid, which produces two secondary traps. The dashed orange curve is the original PSI design which is not monotonic. The solid black line is the new montonic design with the exception for the desired central dip.
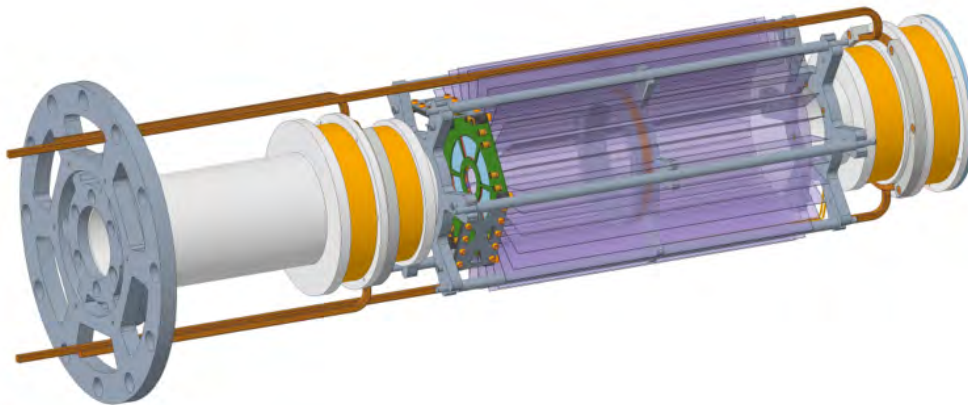

Figure 21: CAD model of the proposed design of the corrector coils and holder system. The coils are shown in gold, the aluminum holders in white and the copper cooling channels in brown. Possible detector arrangements are shown in green and purple. The entire weight is supported from the holder on the left which bolts to an in-vacuum flange plate. The weight of the right section is supported by rods which pass between the radial fins of the detector, at the largest radius possible to avoid blocking muons.

been ordered, and it is in the process of being delivered. The team at RAL have confirmed availability and capability to perform the winding and epoxy impregnation. The design of the holder assembly is provisionally final, barring any major mechanical clashes arising from final configuration of the detector assembly, and quotes are being obtained for the production of the various aluminum holder parts. The delivery of all components to the assembly is due to PSI at the end of Q1 2025.

F.   Superconducting shield

The injection channels plays a crucial role in transporting the muons from the beamline to the bore of the superconducting solenoid magnet. This is done by shielding the muons from the 3 T magnetic field of the superconducting solenoid
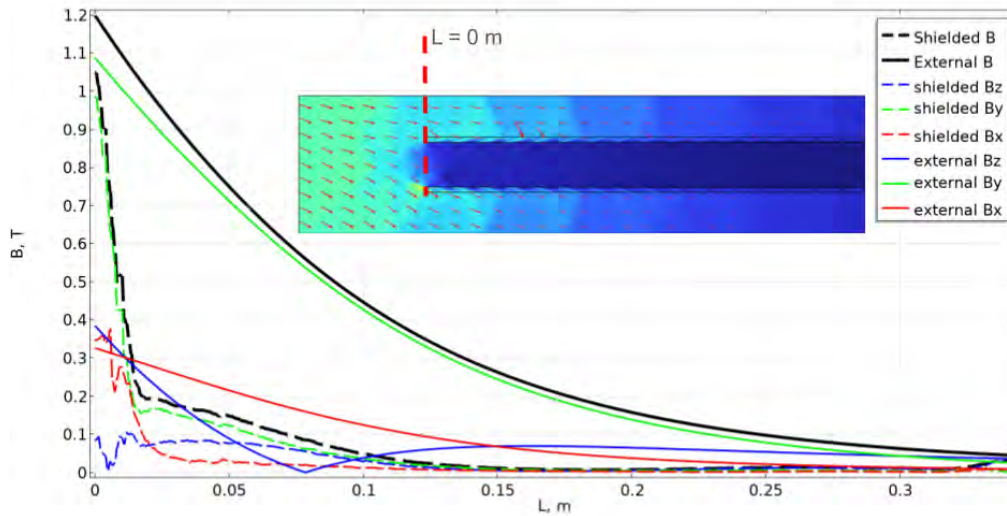
Figure 22: Simulation of shielded and external magnetic field components using COMSOL Multiphysics. Presented are the absolute values of the shielded and external magnetic field components along the axis of the superconducting tube.

using persistent currents induced in the superconductor during the ramp of the solenoid field. The simulation results of the G4 beamline [13] suggest that the mean transverse components of the magnetic field in the local reference frame of the muon must be less than 25 mT to achieve a sufficiently high injection efficiency. The longitudinal components along the reference trajectory of the muons can remain greater because this would cause the muons to spiral along the reference trajectory, thus increasing transmission efficiency.

In order to shield the magnetic field, we investigated the usage of superconducting tubes. Assuming a perfect, 340 mm long superconductor tube with a diameter of 15 mm, we simulated the magnetic field inside using the A-H field formulation with COMSOL Multiphysics (see Fig. 22). We observe a strong decrease in magnetic field inside the superconducting tube, more importantly majority of the tube length shield transverse magnetic field components remain less than 100 mT.

Additionally, by using COMSOL Multiphysics we simulated the cooling of the superconducting tubes using the SRDK-408D2 cold head. The simulation suggests that by using PEEK in the structure supporting the superconductor tube we are able to reach the critical temperature of the superconductors, with 1 W cooling power at 3.9 K of the second stage.

We measured the shielding of the magnetic-field shielding and and the resulting forces when using NbTi and BSCCO2223 bulk superconducting tubes (200 mm length, 15 mm ID and 2 mm thick) at 4.2 K by placing them in a non-uniform but axis-symmetric magnetic field. The BSCCO2223 tube was able to perfectly shield the axial magnetic field up to 140 mT. At an external field of 600 mT we measured a shielding factor of about ten and an axial force of about 6 N. The NbTi tube perfectly shielded the magnetic field up to 160 mT. At 470 mT we measured a shielding factor of about 13 and an axial force of ~4 N.

In 2025 we will assembly a shield made of NbTi/Ti/Cu sheets which has demonstrated superior shielding capacities [14]. In parallel we investigate alternative options made of ReBCO tape wound around a support tube.

G.   Kicker System for test beam times

To deliver pulsed magnetic fields for the September 2024 beamtime, we developed a pulse generator at PSI to approximate the after-pulse oscillations expected from the final system. These oscillations will be constrained by design to less than 10 A per quadrant for frequencies between 100 kHz and 1 MHz to control systematic effects arising from a changing radial magnetic field on the timescale of the muon lifetime [15]. It is during this time after the primary pulse when the muon becomes stored that it is susceptible to the accumulation of longitudinal polarization. Hence, the detectors, especially the SiPMs, must be capable of operating in the electromagnetic environment which persists during this time.

The pulse generator supplied total peak current up to 130 A across the four quadrants of the kicker prototype shown schematically in Fig. 18 connected in parallel (33 A per quadrant). The current discharged from a single low-inductance 5 nF capacitor oscillated with frequency approximately 6 MHz and was damped with an exponential time constant 497 ± 20 ns. It was measured using a wide-band current monitor and is plotted against the LTSPICE simulation of the pulse generator and kicker load in Fig. 23(a). Fast switching was achieved to support the high pulsed current using the OnSemi

NCP81074A low-side MOSFET driver[7] to drive the Infineon IMYH200R012MH SiC MOSFET[8]. This combination, configured on a custom-designed PCB offered short latency of 40 ns and performed reliably without considerable current saturation due to switching losses up to the target operating voltage of 1.5 kV.

This system was operated in September 2024 with a periodic output to supply the 10 A per quadrant necessary to approximate after-pulse oscillations. With the system latency already achieved, it could also be operated in a triggered mode for testing and demonstrating muon storage. The constraints on suppression of after-pulse oscillations, which are being addressed for the final system under development at KIT, are necessary for precision spin measurement but can safely be relaxed for demonstrating muon storage. For kicking muons, the current system would require upgrades to deliver higher peak current with stronger damping. The traces plotted in Fig. 23(b) show measurements taken with

(a) Pulsed Current Oscillation (Sept. 2024), V_{sys} = 1.5 kV

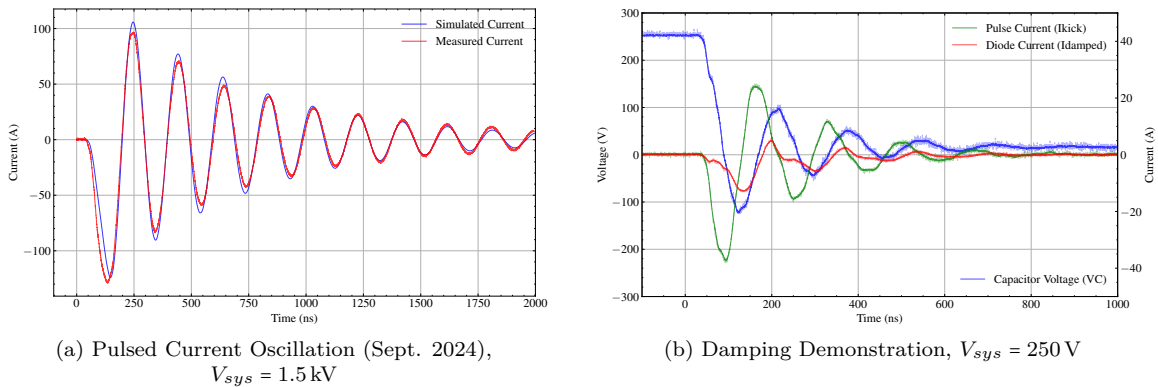(b) Damping Demonstration, V_{sys} = 250 V

Figure 23: The pulse generator developed at PSI supported crucial tests of detectors and electronics in 2024 and offers potential for muon storage demonstration in 2025. A current oscillation up to 130 A per quadrant (33 A per quadrant) is shown in (a), with measurement (red) compared to simulations (blue). An upgraded system would include stronger damping, as demonstrated by the damping element (described in text) giving performance shown in (a) for a system voltage 250 V. The current (green) is damped due to the current diverted (red) through the resistive damping element when the capacitor voltage (blue) is negative.

a damping element added to the pulse generator comprising a reverse-biased GC50MPS33H SiC Schottky diode[9] and 10 Ω resistance given by five 50 Ω ceramic resistors connected in parallel between the diode and ground. The damping element presents a resistive path to ground for the charged capacitor when the voltage drops below zero after the initial discharge. In this way, successive oscillations can be damped without compromising the peak current of the initial pulse. Note that the lower system voltage 250 V was used to allow the diode current to be measured without exceeding probe voltage ratings, but system performance (as seen by the pulse current) was verified up to the nominal voltage 1.5 kV.

When storage simulations were performed using a weakly damped pulse it was found that the successive oscillations can be advantageous when the frequency is matched to the longitudinal betatron oscillation of the muon in the weakly-focusing field. The magnitude of the longitudinal betatron oscillation can be reduced and the storage efficiency improved compared to a single pulse with the same peak current. These simulations show that for the proposed kicker coil design with radius 38 mm a peak current of 50 A and damping time constant of 180 ± 10 ns could realize storage with only a 25% reduction in momentum acceptance compared to a single pulse with 100 A.

Preliminary tests have demonstrated that higher peak current can be achieved by parallelizing the system, running independent discharge capacitors and switches for each quadrant. Lower capacitance would be used to compensate the pulse broadening arising from this configuration, while still providing sufficient charge for the desired peak current. These measurements are consistent with simulations which successfully modeled the existing system, motivating current progress on the PCB design for a full test of the upgraded system. This will enable the system to be employed during the requested beam time in 2025 to demonstrate and characterize the storage of muons in our experiment.

H. Kicker power supply for final muEDM search

The kicking of the muons onto a stable orbit requires a precise magnetic field generated by the anti-Helmholtz coil pair. Thus, a precise current pulse through the coil pair is essential. The pulse generator dedicated to this current pulse

---

[7] https://www.onsemi.com/products/power-management/gate-drivers/NCP81074

[8] https://www.infineon.com/cms/en/product/power/mosfet/silicon-carbide/discretes/imyh200r012m1h/

[9] https://genesicsemi.com/sic-schottky-mps/bare-chip/GC50MPS33-CAL/GC50MPS33-CAL.pdf
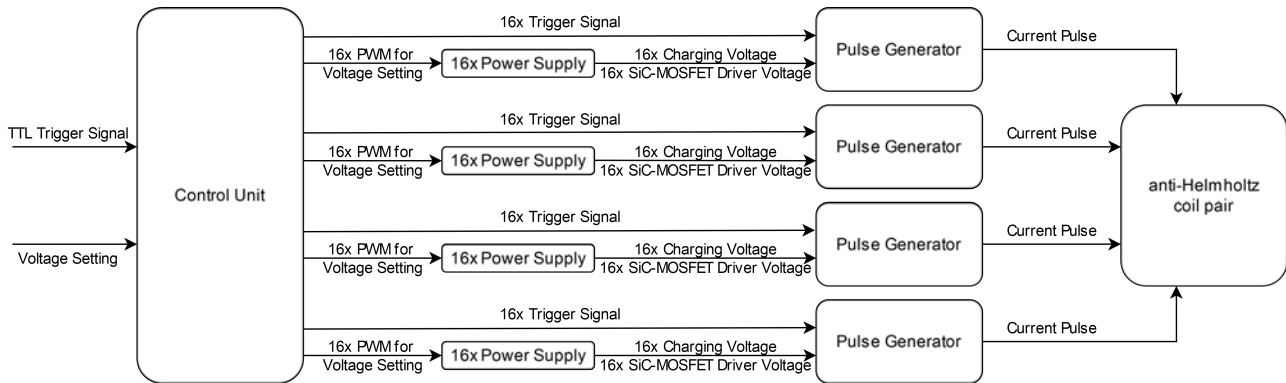
Figure 24: A block diagram of the rough structure of the generator. The TTL trigger signal and the charging voltage setting are provided externally and distributed by the control unit. The voltage setting is provided as a pulse-width modulation to the 16 power supplies per generator. Each power supply provides the charging voltage and switch driver voltage to an individual stage. Each of the 16 stages per generator gets its trigger signal via optical fiber. After triggering, the current pulse travels from the generator to the load.

is being developed to meet the different demands. There are three main requirements and challenges for the generator. The first is the delay between the input of the trigger signal and the beginning of the pulse at the generator output, which must be below 70 ns. The second requirement is the waveform of the current, its peak value of 4×200 A, and the total charge of the pulse, which determines the total change in momentum of the muon. The third challenge is the damping of the waveform, which must be below 10 A after 150 ns to minimize the influence on the muon after it obtains a stable orbit. The diagram in Fig. 24 shows a rough overview of the structure of the generator from the trigger input to the pulse output.

To fulfill the first requirement and for the current to arrive at the coil in time, the delay between the trigger input of the generator and the beginning of the pulse at the generator output must be shorter than 70 ns. At this time, the whole signal path and the pulse triggering must happen. According to the current state of development, the signal path will contain the control unit with an FPGA to distribute the trigger signal to the stages, the fiber optic emitter, fiber, and receiver for transmitting the signals to the stages, and the signal path on the stages to the driver of the switches. In the current design SiC-MOSFETs are used as switches. By applying capacitive gate boosting a decrease of the 10 % to 90 % rise time of a single stage by a factor of $\sim 3 - 4$ to ~ 4 ns was achieved. In general, the delay time between the FPGA output and the start of the pulse, measured for four different stages and four different optical fiber emitters, was below 43 ns. These measurements were taken using a preliminary control unit, consisting of an FPGA evaluation board for the logic and trigger distribution and four PCBs with optical fiber emitters. Also, since the FPGA created the trigger signal without an external source, the signal processing inside the FPGA is not included in the measured time. Additional delay time will be added by different parts, e.g. the signal path from the trigger input to the FPGA. But considering the usual delay times for the different additional parts, e.g. below 10 ns for the FPGA, we expect to achieve a total delay time below the 70 ns boundary.

For the requirement on the current waveform and amplitude, circuit simulations of the coil, transmission line, and a simplified generator were performed on the basis of a model provided by the Paul Scherrer Institute. In these simulations, each coil was supplied by a separate generator. According to the current state of the simulation, the generator voltage must be 12 kV to reach the required peak current amplitude. The current generator design consists of 16 stages in series for each of the four generators. To verify the simulation with measurements, a test stage was developed. It was designed to provide a pulse up to 800 V and 100 A.

The third requirement, the damping of the current, is related to not only the generator but the whole circuit, including the transmission lines, and the anti-Helmholtz coil pair. The inductive load, the capacitors, and the stray inductance and capacitance form a weakly damped oscillating circuit. This leads to oscillations, which must be below 10 A after 150 ns after the pulse begins to reduce their effect on the measurements. In the simulations, the circuit inductance had a large influence on the oscillations. The current investigations concentrate on a generator concept with low inductance that absorbs the reflected wave traveling back from the anti-Helmholtz coil pair. Therefore, in simulations resistors, which sum up the transmission line impedance, were implemented on the stage's outputs. By using a diode in series with these resistors, only the reflected wave after the pulse ends would travel through the resistor and be absorbed there.

Using a single stage and standard power supplies, test pulses were performed up to 800 V. Currently, a power supply to reduce coupling between the stages is under development, and, according to the latest state of development, each stage will get its own power supply. Using the current version of the power supply, measurements up to 350 V were made with up to four stages in series and a 25 Ω load. The recorded waveforms for each of the four stages in the single-stage operation showed good consistency. In addition, the multi-stage operation yielded the expected results. An example voltage waveform of the operation of one to four stages with a 200 V charging voltage is shown in Fig. 25.
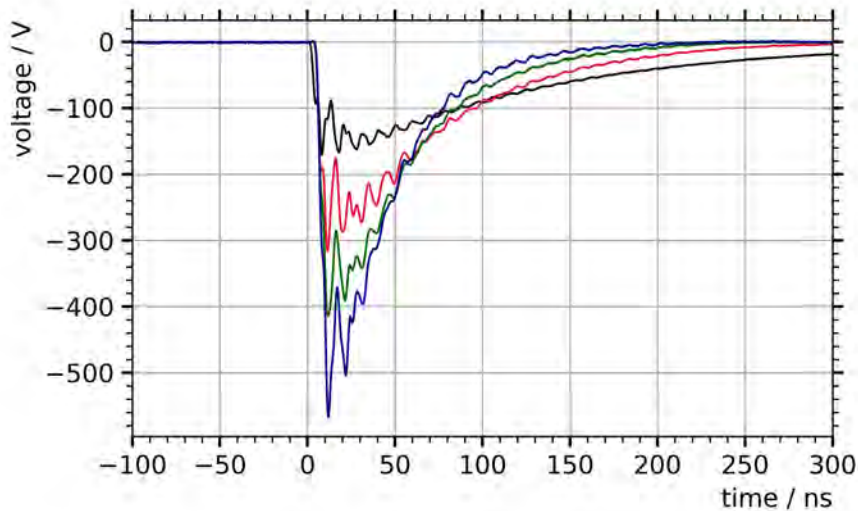
Figure 25: Measured voltage pulses through a $25\,\Omega$ load with a $200\,\text{V}$ charging voltage using one (black), two (red), three (green) and four (blue) of the kicker power supply test stages in series.

I. Muon time projection chamber

For a successful injection of muons into the experimental detector, excellent knowledge and high reproducibility of the muon trajectory are critical. First, achieving high efficiency in trapping muons in the center of the solenoid requires precise positioning of the latter with respect to the beam. Second, the trigger system can work properly only if muons enter the solenoid along a trajectory as close to the nominal one as possible. Finally, cancellation of systematic uncertainties comparing the asymmetries measured with clockwise and anticlockwise injection requires a very small momentum difference in the two running modes, below $0.5\,\%$.

A detailed characterization of the muon trajectories, to be performed before starting the experiment with a dedicated muon tracking detector, would permit identification of a possible misalignment and determination of the average trajectory parameters that are needed to suppress the systematic uncertainties. For muons at $28\,\text{MeV}/c$, these measurements will be greatly affected by the interaction with the detector material (multiple Coulomb scattering and energy loss), and therefore extremely light detectors should be used, gaseous detectors being the most natural choice.

The proposed solution is a Time Projection Chamber (TPC) operated with an extremely light gas mixture based on helium, separated from the vacuum in the magnet bore by an extremely thin and vacuum-tight window ($300\,\text{nm}$ Silicon Nitride). As a read-out structure for this TPC, the GridPix detector is considered. GridPix is a gaseous detector made of a conductive mesh implanted $50\,\mu\text{m}$ above a Timepix chip [16]. A voltage difference between the mesh and the chip produces an avalanche when drift electrons reach the mesh, so that the GridPix behaves like a sort of microscopic Micromegas.

After a laboratory and beam test campaign in 2022 and 2023, that demonstrated how a GridPix TPC with helium-isobutane mixture is suitable for tracking muons in the muEDM environment [17], in 2024 we completed the conceptual design of the detector, performing simulation studies tuned on the final configuration of the beam to be used in the phase I experiment. We converged on a conventional configuration in which the TPC is a cylindrical chamber with a drift field along its axis, parallel to the main component of the magnetic field.

In Fig. 26 we show the expected momentum resolution and the comparison of true and reconstructed phase-space coordinates at the exit of the injection channel. A momentum resolution better than $0.4\,\%$ may be obtained, and the phase space resolutions look sufficient for alignment purposes. Here we assume to operate the detector with an absolute gas pressure of $0.4\,\text{bar}$. In case of detector problems at such low pressure, operating at atmospheric pressure, as in beam tests, would still allow for reaching $0.5\,\%$ momentum resolution.

We verified the compatibility of the chosen configuration with the technical design of the holder system depicted in Fig. 21), and the technical design of the TPC is currently on-going. We aim to build and test the detector within Fall 2025, in order to use it in the requested beam time at the end of the year.

J. Muon Injection trigger

In Phase I, only about 4×10^{-3} of the muons that have passed through the magnetically shielded injection channel (see Section II A 1) are on or close to a spiral trajectory that may result in storage. Any other muon needs to be vetoed
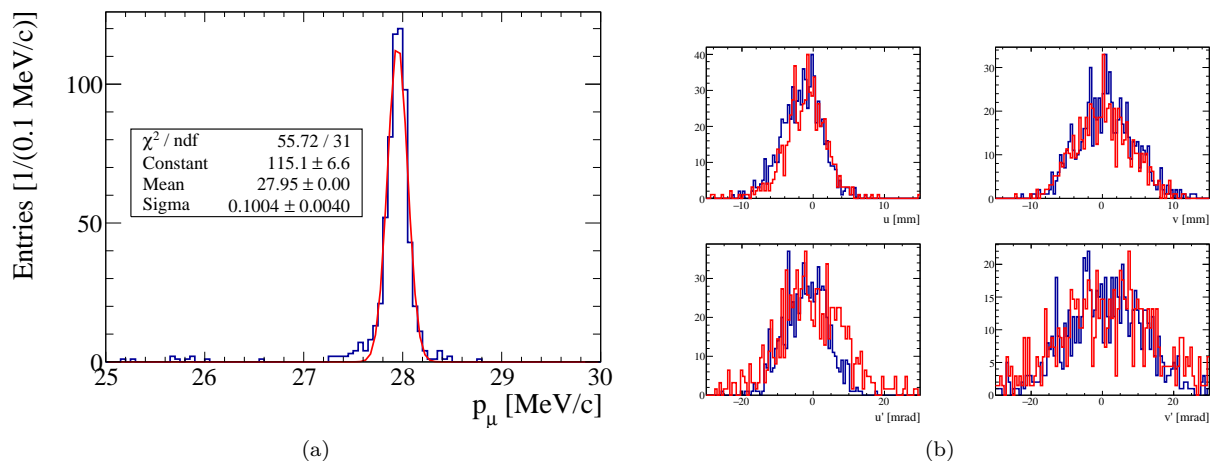
Figure 26: Performance of a longitudinal TPC for the reconstruction of injected muons. (a) Reconstructed momentum (assuming 28 MeV/c initial momentum). (b) True (blue) and reconstructed (red) phase space coordinates and angles (u: horizontal; v: vertical).
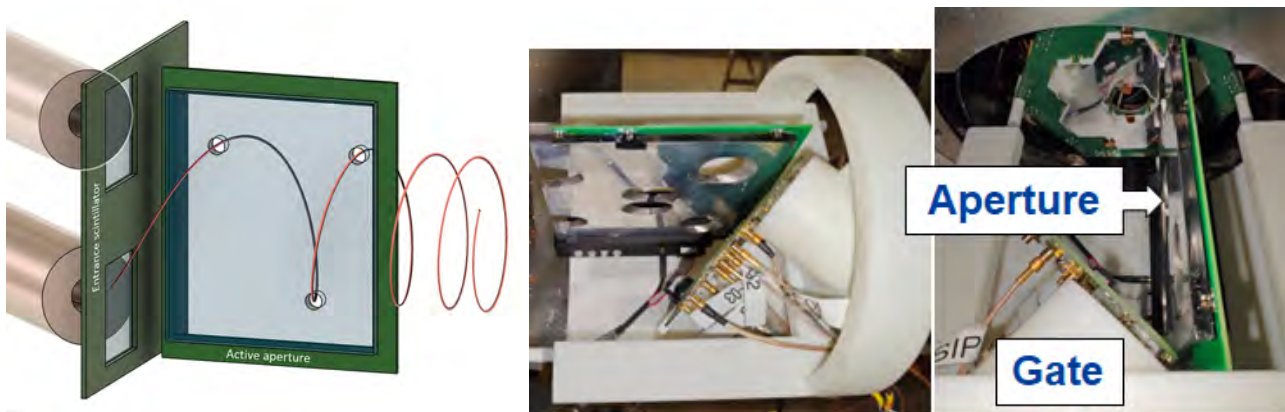

Figure 27: Left: CAD sketch of the entrance trigger. On the left, the muons exit the collimation tube shielded by a super-conducting shield. The strong magnetic field immediately bends the muons onto a spiral trajectory. First, they pass through a thin 100 μm gate scintillator. A thick second scintillator forms an active aperture, with holes at positions along the reference muon trajectory, which stops and detects muons that are outside the acceptance phase space. A trigger for the magnetic pulse (see Sec. II H) will only be generated in the case of an anti-coincidence between the gate scintillator and the active-aperture scintillator. Right: A fabricated trigger detector.

to avoid triggering magnetic kicks that, in any event, would not store muons.

The muon entrance trigger generates a signal triggering the magnetic kick at the right moment when the muon passes the weakly-focusing field region (approximately 80 ns after having left the injection channel). It is made of two thin scintillator tiles, 100 μm-thick gate scintillators, one each at the exit of the CW and CCW injection tube, in combination with an active aperture made of a scintillator approximately 5 mm thick, aka anti-coincidence scintillator (ACS). which has holes around the reference muon trajectory. The anti-coincidence between the thin gate scintillator and thick active aperture is used to create a TTL-signal to trigger a pulsed magnetic kick to deflect the trajectory of the muon onto a storage orbit. Due to this, the pulse rate of the kicker power supply reduces from about $12 \times 10^4 \, \mathrm{s}^{-1}$ to $500 \, \mathrm{s}^{-1}$. Figure 27 shows the CAD of the entrance detector with the injection trajectory.

Simulation studies emphasize the need for pulse latency within a narrow window of 120 ns to 150 ns, between muon detection and the rising edge of the magnetic pulse. By designing a high-speed SiPM readout electronic circuit to generate the TTL signal, we could demonstrate a propagation delay of less than 5 ns. This alleviates the demand for the internal delay of the HV kicker current supply, as various elements, i.e. TTL and pulse transmission lines, contribute.

The design of the Phase I entrance detector electronics is being studied using the electronic simulation tool LTSPICE, as well as Geant4-based simulation tools such as musrSim and G4beamline. The schematic diagrams of the entrance
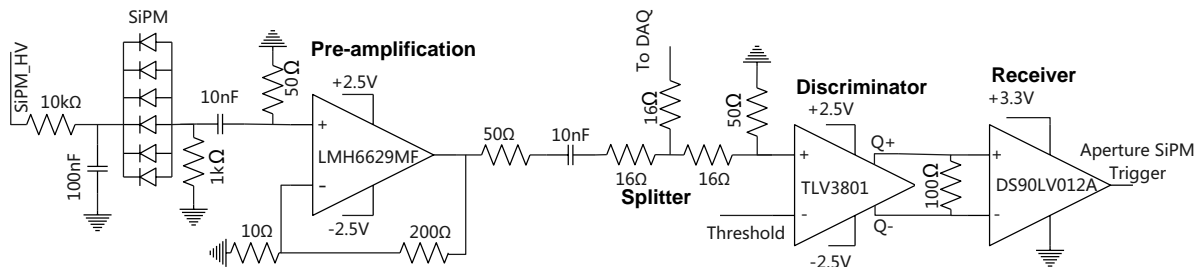
detector electronics, shown in Fig. 28, comprise four main components: the DC-DC step-up converter, gate electronics, aperture electronics, and anti-coincidence electronics.
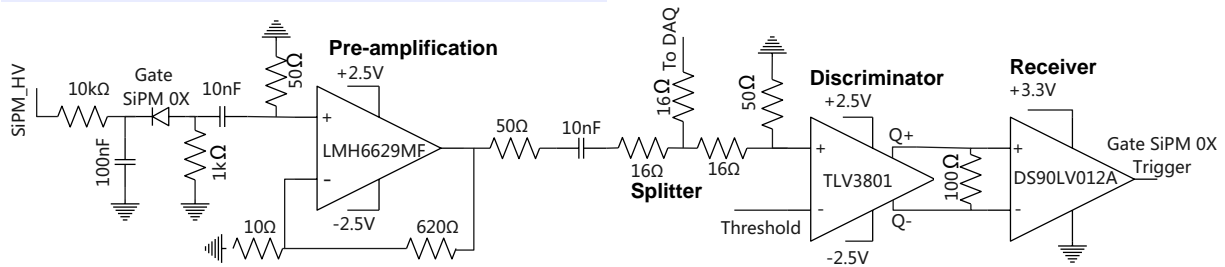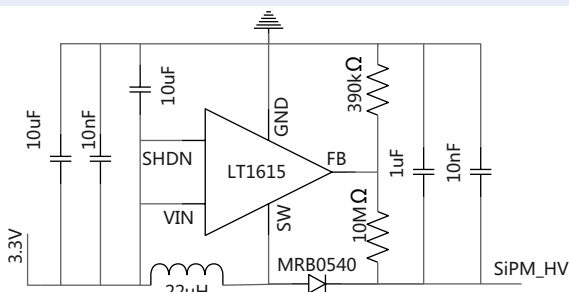

(a) Gate detector readout circuit

(b) Aperture detector readout circuit

(c) Electronics for the DC-DC Setup Converter
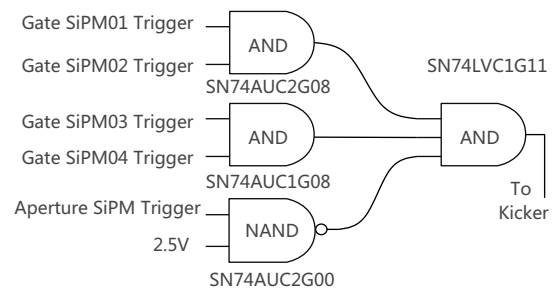
(d) Anti-Coincidence Circuit

Figure 28: Simplified schematic of the SiPM readout.

The circuits for the gate and aperture electronics are similar in design, with the primary distinction being their SiPM configurations. The gate electronic is connected to a single SiPM, whereas the aperture electronic integrates six SiPMs connected in parallel, producing a single output. The gate detector uses four SiPMs for clockwise (CW) and counterclockwise (CCW) injection, respectively. However, the design requires CW/CCW readout to share electrical channels, necessitating four gate electronic modules. In contrast, the aperture detector requires only a single aperture electronics channel.

Prototype boards for the readout electronics have been fabricated based on the schematic diagrams shown in Fig. 29. The gate board features two windows to facilitate muon injection from both Clockwise (CW) and Counterclockwise (CCW). Each window contains an ultra-thin scintillator slice with dimensions of $20 \times 20 \times 0.1, \mathrm{mm}^3$ (EJ200), enclosed within a $25 \times 25 \times 5, \mathrm{mm}^3$ acrylic light guide. The light guide is custom-fabricated in-house in Shanghai Lab using Computer Numerical Control (CNC) drilling and grinding techniques to enhance photon collection efficiency. Four Silicon Photomultipliers (SiPMs) are mounted at the center of each of the four sides of the light guide using BC-603 optical grease, ensuring effective detection of the collected photons.

Additionally, the gate PCB integrates two switches into the SiPM power supply and signal readout circuits, allowing seamless activation and deactivation of the corresponding SiPMs for CW and CCW modes. This design enables the CW and CCW SiPMs to share a single set of readout channels, reducing the total number of electronic channels required from 8 to 4. This streamlined configuration enhances the system's efficiency while maintaining optimal performance.

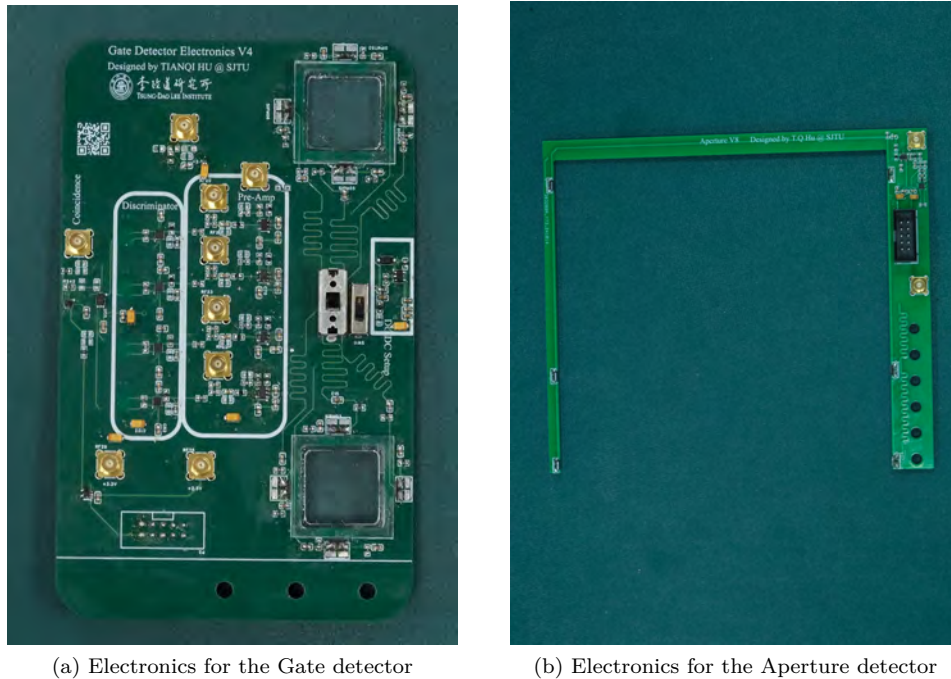(a) Electronics for the Gate detector   (b) Electronics for the Aperture detector

Figure 29: Electronics prototype for the entrance detector

The aperture electronics board is tailored to match the dimensions of the aperture scintillator ($(130 \times 135 \times 5, \mathrm{mm}^3)$, with six SiPMs strategically positioned along the edges to maximize photon collection, as determined through simulation. The SiPMs are connected in parallel with a single output, minimizing the number of required channels. Communication between the aperture and gate detectors is facilitated by ribbon cables, while the anti-coincidence circuit is seamlessly integrated into the gate detector's circuit board to efficiently manage both coincidence and anti-coincidence operations.

K. Frozen-spin electrodes

The design of a new prototype for the frozen-spin electrodes is advancing towards the construction of a complete electromagnetic test system. Such a system will be used to conduct in-vacuum tests to verify electric field stability and in the testing of prototypes of the pulsed power supply in development at KIT. The design, shown in Figure 30a) builds upon the experience gained in the construction of earlier prototypes using thin metalized films which were developed cooperatively with the DIAPP Group of LTP. A Kapton film of 80μm is permissible in view of the expected material budget which will be dominated by the scintillating fibers and kicker coil. Thicker films offer greater rigidity and robustness against creasing, although their elasticity can generate stress in the film which may disrupt the desired cylindrical form. This effect is overcome by implementing a spiral seam rather than a linear one, such that the hoop stress is partially transferred into the longitudinal axis which is better compensated by the fixed end supports.

The outer electrode ($r = 25$ mm) will be held at ground and the inner ($r = 35$ mm) charged to high voltage of 1.8 kV/cm. The metallisation will be distributed in 2 mm wide strips with pitch 4 mm running parallel to the spiral seam. The total length of this metallisation along the longitudinal axis will be 300 mm. Two fabrication methods are currently being investigated and procured for testing: laser engraving and flexible PCBs. The former could be achieved through precision ablation of a 30 nm aluminum coating on a uniformly aluminised Kapton film of thickness $50\,\mu$m. The latter would be fabricated with a $12\,\mu$m copper deposit. The flexible PCB would allow vias to connect the front and back layers to ensure secure contact with the aluminum end supports. The proposed design will be used to support vacuum and electrical tests, while also informing future iterations to refine the design further for mechanical integration and ultimately commissioning in the experimental apparatus in 2026.
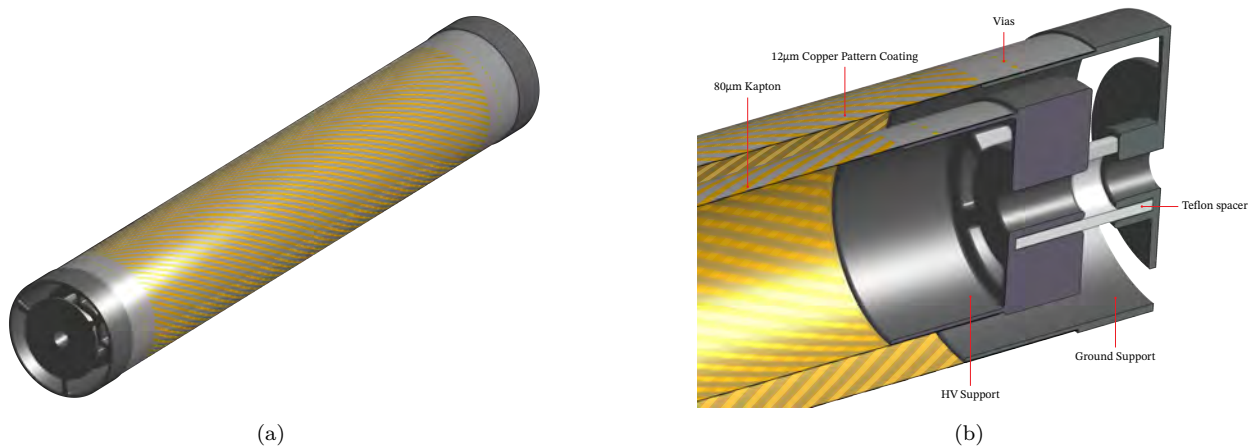
Figure 30: A new prototype electrode system will be used for tests of electric field stability in vacuum and in tests of the pulsed power supply for the kicker. (a) Ground and HV electrodes feature a spiral seam and striped pattern of metallisation on an $80\,\mu$m Kapton film. The end support structures, detailed in (b), are mechanically connected with a teflon spacer such that the inner HV electrode is fixed relative to the outer ground electrode.
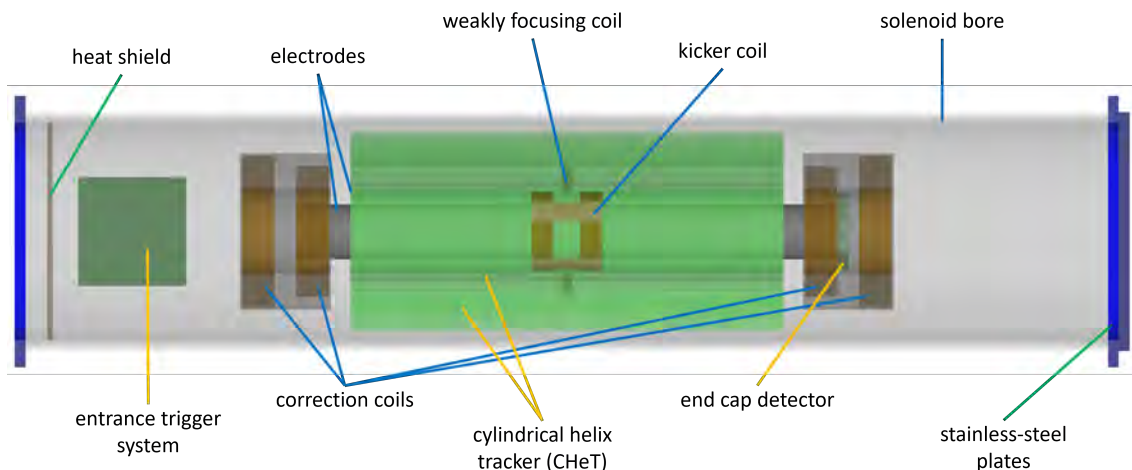

Figure 31: Geometry implemented in the GEANT4 simulation. The muons enter from the left through the injection channel (not shown here).

L. Update design positron detection

A detailed model of the experiment in GEANT4, shown in Fig. 31, permits the study of positron decays from muons stored in the trap but also from muons stopped at the entrance trigger detector.

The critical aspect of the muon EDM search is the ability to measure the direction of the outgoing positron. This holds true for the three sequential steps of the experiment: demonstrating muon storage, measuring $g-2$ frequency as a function of the electric field, and acquiring EDM data with an electric field matched to the frozen-spin condition. The kinematics of an e^+ coming from decay is described in Ref. [18]. A significant positron background is generated by stopping muons in the ACS. As the expected injection efficiency is approximately 0.45%, 99.55% of the muons are being stopped and decay in the ACS, emitting positrons. A fraction of these will produce a non-correlated background in the positron detector. Simulations of the three distinct measurements and the positron background provide the specifications for the positron tracker:

Momentum resolution around a few MeV/c, necessary for selection cuts on positron momentum to increase the sensitivity to the change in asymmetry in a momentum binned analysis, see also Ref. [18];

Single-hit resolution around 1 mm, necessary to reconstruct tracks with the required angular resolution for a higher
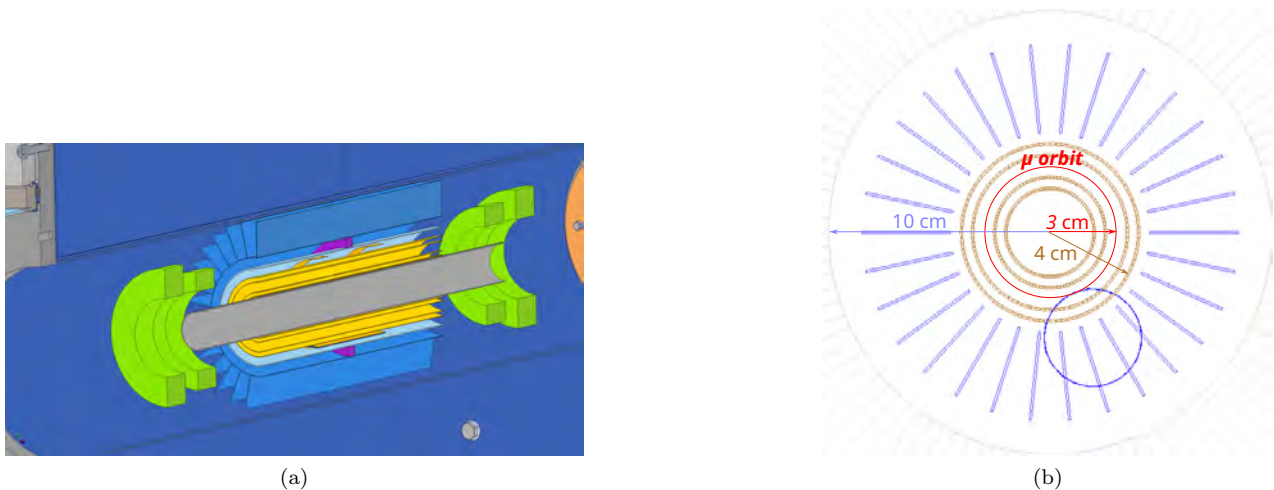
Figure 32: (a) A 3D view of the CHeT detector inside the magnet. (b) Frontal projection of the CHeT with highlighted sizes and a simulated event shown for reference. The longitudinal size of the detector extends for 400 mm.
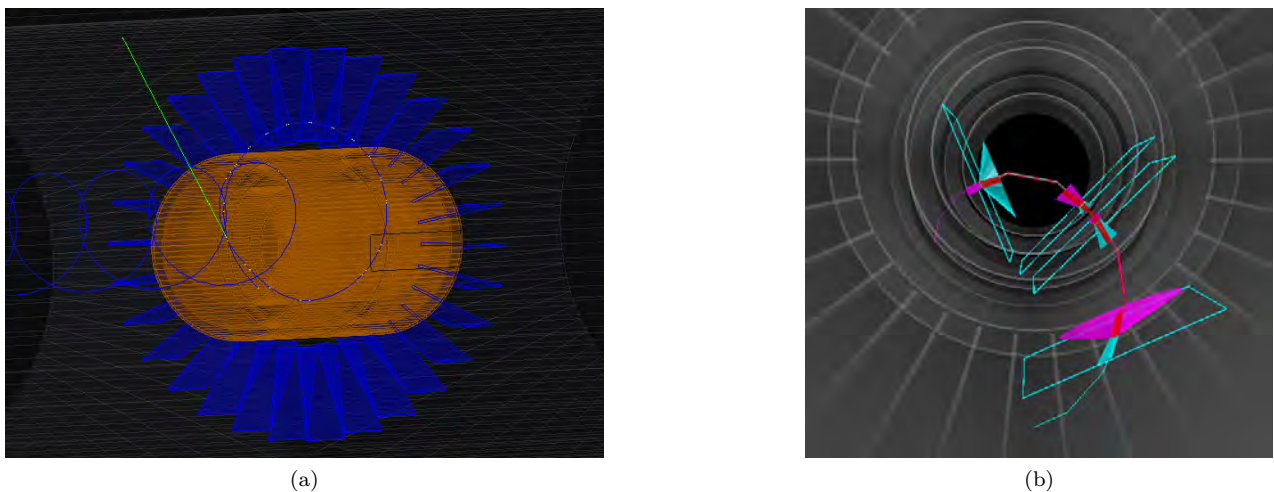

Figure 33: (a) GEANT4 simulation of a positron event inside the CHeT detector; (b) GENFIT event display of a fitted positron track.

sensitivity to a change in asymmetry.

Timing resolution less than 1 ns, necessary to separate different hits produced by the same positron when it curls through the detector. Positrons from muon decays travel approximately at c, meaning that in the expected magnetic field a complete circle in the transverse plane takes $\gtrsim 0.6$ ns, imposing a limit on the time resolution.

To meet these specifications we will deploy the Cylindrical Helix Tracker (CHeT) in Phase I. Figure 32a) shows a computer-aided detector design. It consists of two concentric cylinders inside the high voltage electrode, $r = 20, 24$ mm, and two concentric cylinders outside the ground electrode, $r = 37, 40$ mm, made of scintillating fibers of 500 μm diameter, coupled to SiPMs. Each cylinder consists of two stereo layers of scintillating fibers to precisely measure the position of the positron hit on the detector. These scintillating fiber cylinders are complemented by 30 tiles, depicted in blue in Fig. 32a, each comprising two layers of orthogonal scintillating fibers for the precise measurement of the radial and longitudinal coordinates of the hits.

The tiles are important in the first phase of the experiment when the $(g-2)$ precession will be measured, since they allow the measurement of the decay angle of the positrons in the muon orbit plane with a resolution of a few milliradians. The cylinders are deployed as near to the muon orbit as possible, which is essential to detect decay positrons emitted almost parallel to the magnetic field with a small curvature radius, which are most sensitive to a muEDM.

This design allows for fast, versatile, modular, and low-cost detector technology to be operational in large magnetic
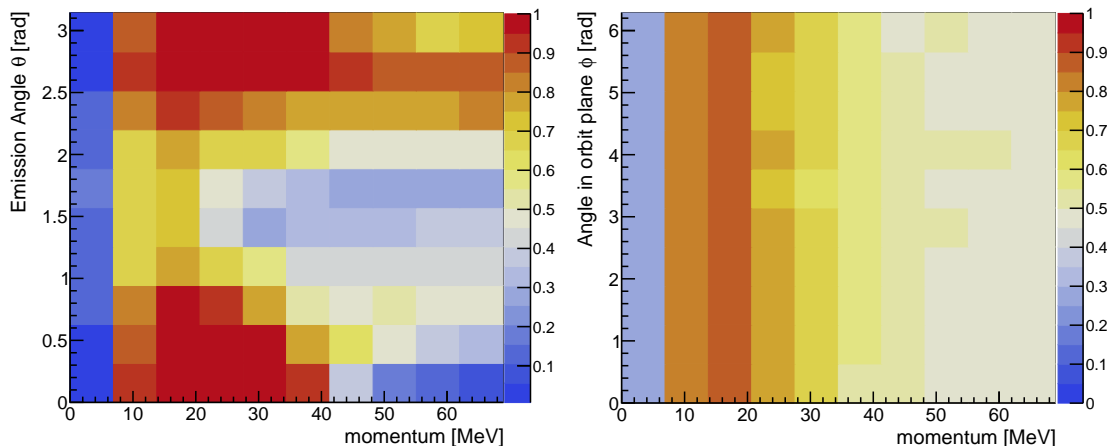
Figure 34: CHeT acceptance as a function of momentum and θ and momentum and ϕ. While the acceptance in ϕ is flat because of the detector cylindrical symmetry, in θ the acceptance is maximum for $\theta \sim 0$ and π: this correspond to particles emitted perpendicular to the magnetic field.

Table V: Achieved resolutions in a simulation of the CHeT detector.

Variable	Resolution
σ_p/p	0.05
σ_θ	10 mrad to 30 mrad
σ_ϕ	3 mrad

fields and in vacuum and adheres to the geometrical constraints imposed by the frozen-spin electrodes, the kicker, the weakly focusing coils, and their support structures. With 500 µm fibers, this detector design requires approximately 200 meters of fibers and 2000 read-out channels, assuming that 4 fibers are coupled per SiPM. This reduction in the number of readout channels ensures a spatial resolution better than 1 mm in the $x - y$ coordinates.

The detector's acceptance and resolutions of the kinematical variables were evaluated through a GEANT4 simulation. The bi-dimensional distributions of the acceptance are shown in Fig. 34, while the average resolutions are summarized in Tab. V.

M.   A dedicated data acquisition for muEDM

The data acquisition (DAQ) system of muEDM is tasked with collecting data on hits and rates from various scintillation detectors, including the positron tracker, trigger entry window, and beam monitors. These data will be used for event reconstruction and to assess the stability of the system. The number of read-out channels is on the order of 1000. The trigger signal opens a gate in which any hit occurring in the positron tracker and in the scintillation trigger window must be registered to fetch the positron tracks emerging from the muon decay. The inclusion of the trigger window is also important for tracking possible pile-up muons in the time window. A ChET scintillation fiber is read out by silicon photo multipliers. Since the expected integrated rate in the positron tracker is on the order of a few kHz, the probability of having more than one positron track in a gate is not negligible; all of them must be registered by the DAQ. The chosen solution is the CAEN FERS A5202. The A5202 is equipped with two Weeroc Citiroc-1A ASICs, offering exceptional performance and versatility in data acquisition. Its on-board A7585D SiPM power supply ensures precise biasing of the sensors, facilitating optimal operation and reliable data collection. It provides multiple acquisition modes such as charge integration (energy measurements), counting (rate measurements), and timing, with multiple hit time-to-digital conversion (TDC) and time-over-threshold (ToT) capabilities, providing a resolution of approximately 250 ps. The maximum read-out rate is greater than 10 kHz, as specified in the data sheet. Thus, it covers all the above-mentioned experimental needs, including Phase II. Scalability is a key feature of A5202, allowing the management and synchronization of up to 128 cards, i.e., 8192 channels, by a single DT5215 concentrator board. This seamless integration is made possible through the utilization of optical TDlink technology, ensuring efficient data transfer and synchronization across multiple channels. The configuration and testing of the DAQ system were crucial steps to ensure the proper functioning of the setup. The initial test was performed in Pisa with a simple configuration of a naked SiPM to assess the capability to measure the sensor dark rate. We developed an optimal configuration in terms of cable shielding
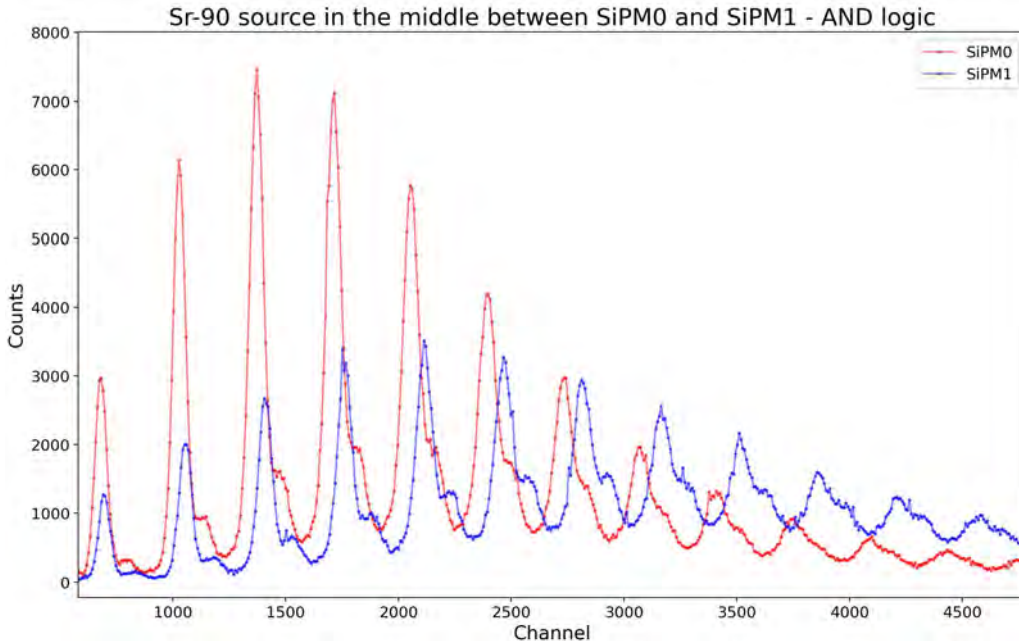
Figure 35: Charge spectra of two SiPMs connected to a one meter long fiber irradiated at its center. The trigger is on the coincidence of the two sensors with a threshold at one p.e. level. Both signal distribution are significantly above the noise level.

and noise reduction that was exploited in a more realistic set-up at PSI with a one meter fiber read by two SiPMs at both sides. As visible in Fig. 35 the signals emerge over the threshold set to a level of one photo electron.

This marked a significant milestone, confirming that the set-up could reliably measure signals under controlled conditions. During 2025, we will test different possible connections between SiPM and FERS using both shielded cables and PCB to move from two channels to several channels. In addition, MIDAS will be used as the DAQ software framework and the A5202 readout software will be imported into MIDAS. Although challenging, similar integrations have been already implemented for other experiments. MIDAS includes slow control modes, readout options, and other trigger and calibration capabilities and is already adopted by many experiments as a DAQ.

III.   ANALYSIS OF TEST BEAM 2023 FOR MUON TOF

In this section, we present the experimental results of the test beam measurement on piE1 in December 2023 for the muon time of flight (ToF). The main goal of this test beam was to study a systematic effect from a change of the momentum of injected muons for magnetic fields with different polarities and magnitude.

In the experimental setup, the muons exiting the beamline travel through some air before entering the PSC magnet bore through an injection channel. For the injection channels, we used magnetic steel tubes to shield the magnetic field of the solenoid. The distance between the detector upstream (US) at the entrance and downstream (DS) at the exit of the tube is d_{US-DS} = 1158.15 mm, respectively d_{US-DS} = 1164.20 mm after a change in setup. ToF measurements were taken for different detector sets and at different magnetic fields in the range of ±750 mT. In addition, there are two other data sets in which the slit opening of FSH52 and the position of the PSC magnet were scanned. The ToF detectors have scintillating foil thicknesses of 200 µm (Detector #0), 100 µm (Detector #1 and #2) and 50 µm (Detector #3 and #4) and were mounted in five different configurations: US#0-DS#1, US#2-DS#1, US#3-DS#1, US#4-DS#3 and US#4-DS#1. There are four SiPMs for each detector, which is provided with a voltage of ≈ 220 V for each channel by the standalone wavedream board. The waveDAQ records the waveforms for each channel and its maximum rate is 5 GSamples/s.

The waveforms of the detectors were analyzed as follows. In a first step, the waveforms of all four SiPMs of a detector were summed. Thereby, reducing noise seen by just one SiPM and also considering the SipM that saw the signal first. A time window, in which to search for the zero crossing of the constant fraction discriminated signal, is chosen by fitting the times of the pulse minima of the whole data set to a Gaussian. Afterwards, a constant fraction discrimination (CFD) is performed for the summed waveforms of the upstream and downstream detectors. The fraction and delay were optimized by scanning a range of values for a data set where the detectors were right next to each other (short configuration). The optimal parameters for each detector were then found by searching for the minima of $\sigma^2/\sqrt{N}$ where σ is the standard deviation of the ToF distribution and N is the number of extracted ToF values. The time of flight values are extracted
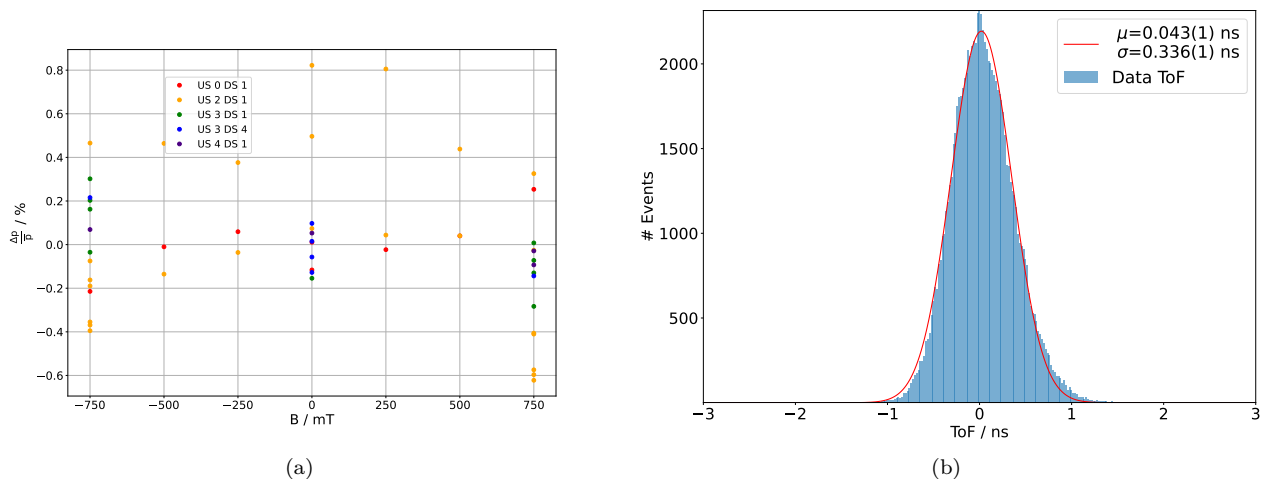
(a)

(b)

Figure 36: Figure 36a (left) shows the difference in mean muon momentum for all detector sets scanning over the B field. Figure 36b (right) shows the ToF distribution in the short configuration for detector #4 giving the timing resolution of 336 ps.

by subtracting the times of the zero crossings and give rise to the ToF distribution. The distributions are fitted to a double exponentially modified Gaussian (DEMG), the simple exponentially modified Gaussian (EMG) is of the form

$$f(x) = \frac{\lambda}{2} e^{\frac{\lambda}{2}\left(2\mu + \lambda\sigma^2 - 2x\right)} \text{erfc}\left(\frac{\mu + \lambda\sigma^2 - x}{\sqrt{2}\sigma}\right) \tag{8}$$

where μ and σ correspond to the mean and standard deviation of the Gaussian part of the distribution and λ is the decay constant.

To be able to calculate the muon momenta from the ToF values, measurements with positrons for the different sets were performed at 0 mT. Only for detector configuration US#4-DS#1 there is no reference measurement with positrons. Taking into account the distance between the detectors and the fact that positrons at these energies travel almost at the speed of light ($\beta \approx 1$), they can be used as a reference to extract the time offset of the system. The distribution of the positrons is then fitted to a Gaussian to find the mean. The error on the mean muon momentum is calculated by using error propagation and errors on the mean for both fits and considering an error of 0.1 mm in measuring the distance between the detectors. Figure 36a shows the deviation of the mean muon momentum of each detector set for measurements at various magnetic field values.

Furthermore, the timing resolution of the detectors in the short configuration was studied by calculating the standard deviation of the distribution. Figure 36b shows the timing resolution for the 50 µm detector #4 of 336 ps going down to 265 ps for the other 50 µm and 100 µm detector.

IV.   TEST BEAMS 2024

A.   muE1 - characterization

In June 2024 we characterized the μE1 beamline in Z-configuration. The beam was tuned to obtain the highest rates, and measurements were made for muon momenta of 100 MeV/c and 125 MeV/c from backward decays of pions at 173 MeV/c and 216 MeV/c momenta. In addition we looked at muons with momentum of 140 MeV/c from foward decays of pions at 127 MeV/c. These measurements were made using a 'Scintillation Fiber' (SciFi) detector and a Lanthanum Bromide (LaBr) calorimeter with two crossed scintillation bars (SciCross) in coincidence. Quadrupole scans using the the last two quadrupoles, QSK810 and QSK811, were performed to extract the 4D phase space followed by 3D rate scans using the SciCross-LaBr detector mounted on an XYZ table for the energy spread and dispersion measurements. The results of the 125 MeV/c muons are displayed here and the other results will be made available upon request. The data from the quadrupole scans [20] were analysed to extract the 4D phase space shown in Fig. 39 as phase space ellipses[21]. Using data from the SciCross-LaBr detector, the resolution of the LaBr, the Time-of-Flight (ToF) distribution and phase uncertainty (Fig 40), and the energy spread and the horizontal energy dispersion (Fig 41) were obtained. The efforts to model the obtained results in G4beamline and XSuite (Python) are underway.

(a)   (b)
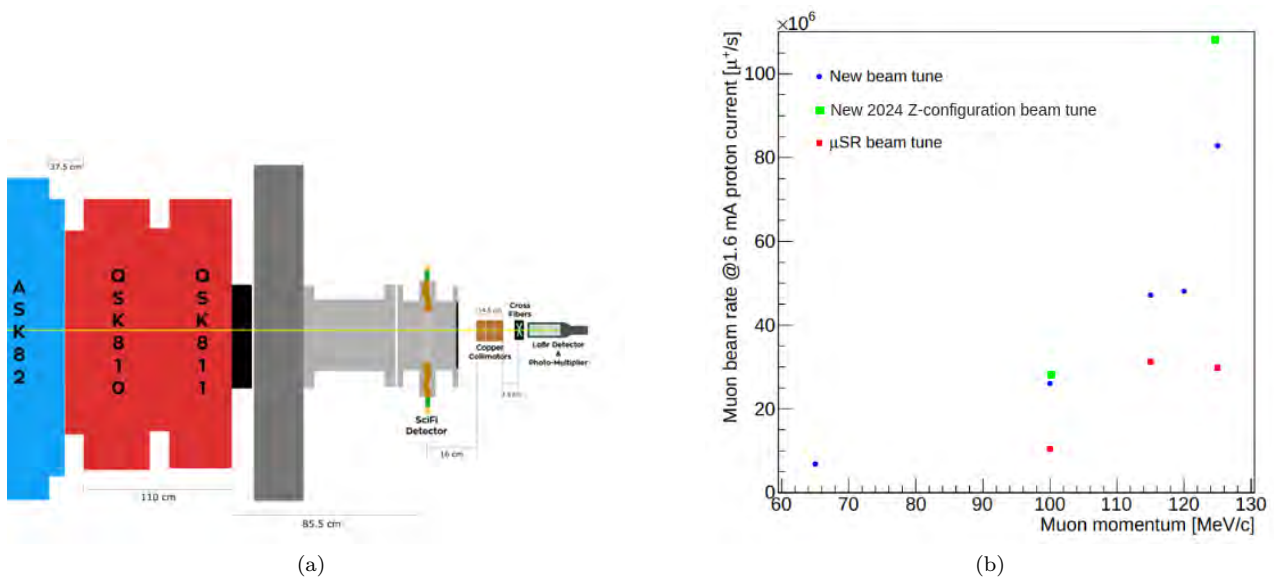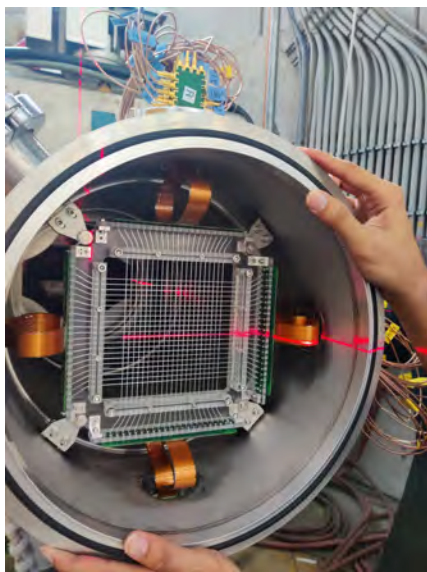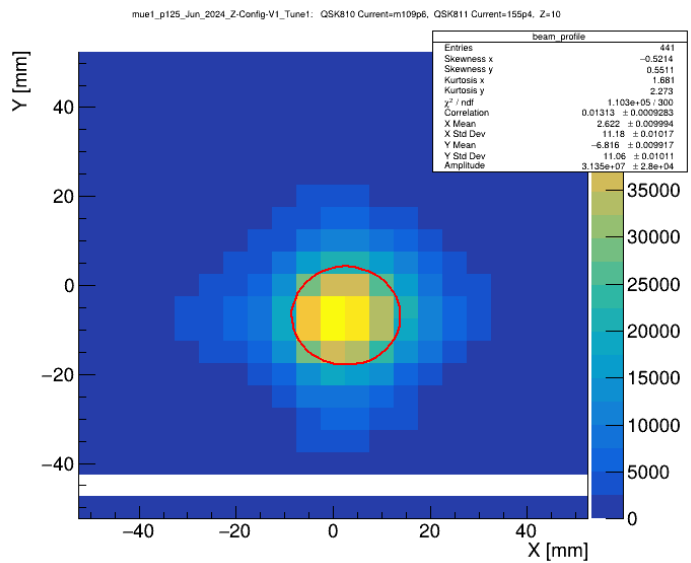
Figure 37: (a) Experimental Setup. (b) Higher rates were observed in June when compared to the U-configuration by M. Sakurai[19]

(a)   (b)

Figure 38: (a) SciFi detector during mounting using a laser for alignment. (b) Transverse beamspot for 125 MeV/c muon momentum.

B.   piM1 - muon detection and pulser operation

It is necessary to keep the relative positron detection efficiency constant, for both positrons spiraling along or opposite of the main magnetic field direction, to avoid any systematic effects. A potential challenge is related to the strong magnetic pulse used to kick the muons onto a stable storage orbit, which naturally introduces early-to-late changes in the magnetic field and through that possibly in the measurement system as well. The primary goal of this beam time was the validation of a scintillator-based positron detection system that meets the stringent temporal stability requirements of the muon EDM experiment.

The experiment was set up on the PiM1 beamline, using stopped pions in a target as a source of Michel decay positrons.

(a)

(b)
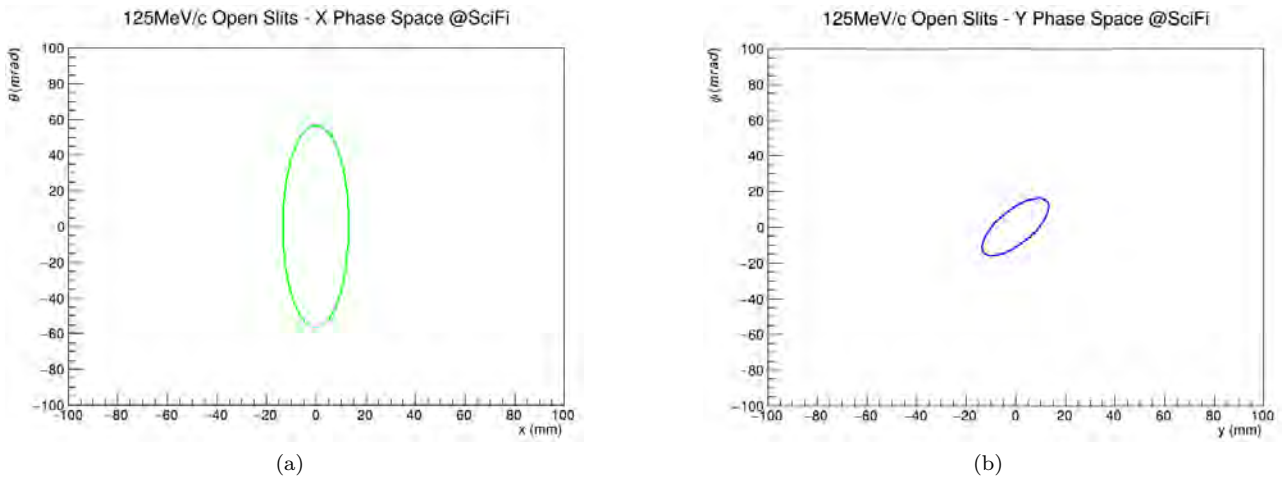
Figure 39: Phase space for 125 MeV/c muons. (a) X phase space, (b) Y phase space.

(a)

(b)
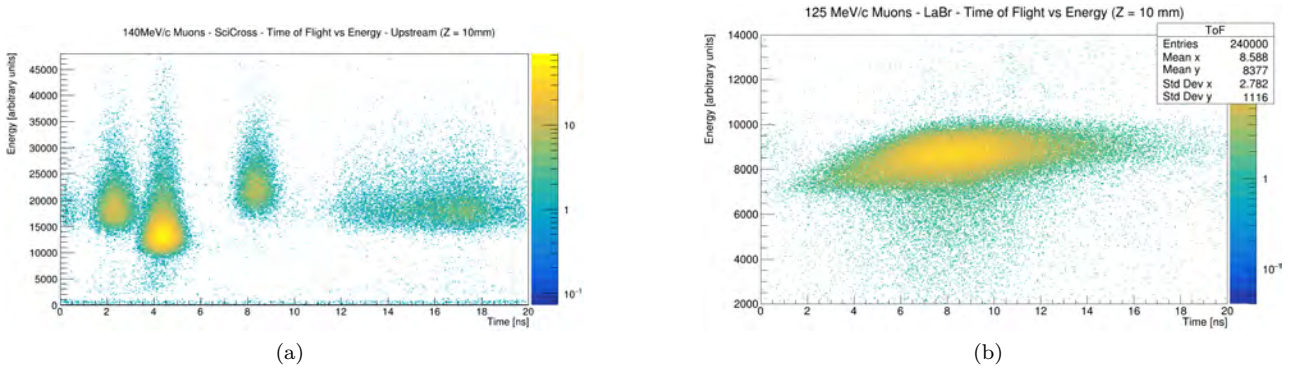
Figure 40: (a) ToF spectrum of muons with 140 MeV/c momentum from forward decaying pions. (b) ToF spread of muons with 125 MeV/c momenta, resulting in a spread of 2.78 ns.

(a)

(b)
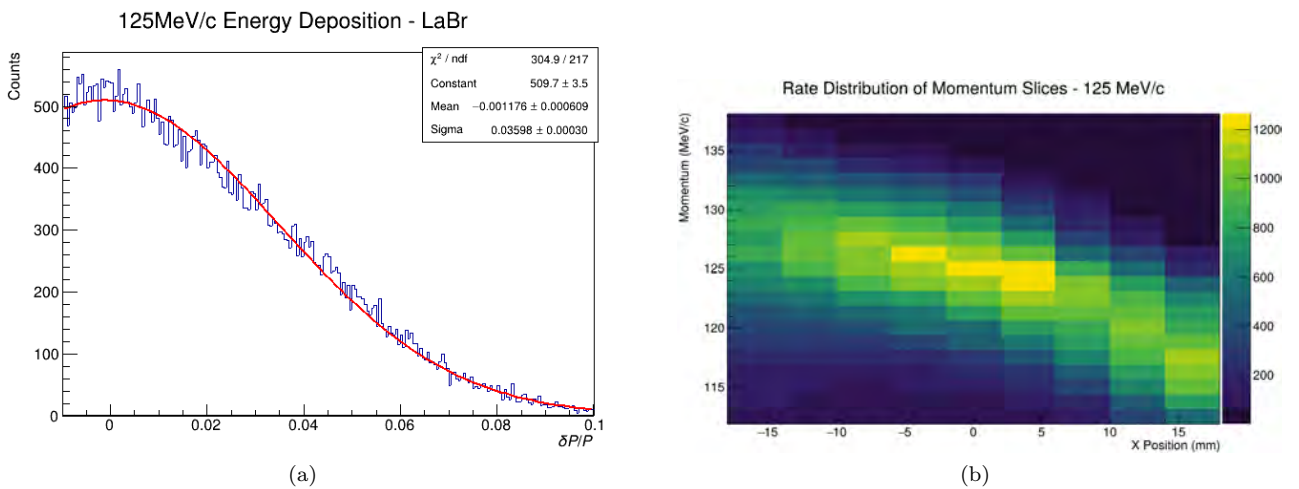
Figure 41: (a) Momentum spread of muons with 125 MeV/c central momentum, $\frac{\Delta P}{P} = (3.41 \pm 0.20)\%$. (b) Muon beam horizontal energy dispersion for 125 MeV/c central momentum, $D(\delta) = (-79.90 \pm 6.63)$MeV/$c$/mm.

Figure 42: Top view of the experimental setup showcasing the copper collimators on the right, the plastic target in the middle, the magnetic kicker surrounding the target and connected to four co-axial cables, and the two symmetrical hex scintillation detector boards.

Figure 43: Hexagonal detectors front and back side view.

The pions exiting the beamline were degraded in $8\,\text{cm}$ of copper. The beam was collimated before entering the bore of the superconducting magnet with a copper aperture. The remaining pions with a mom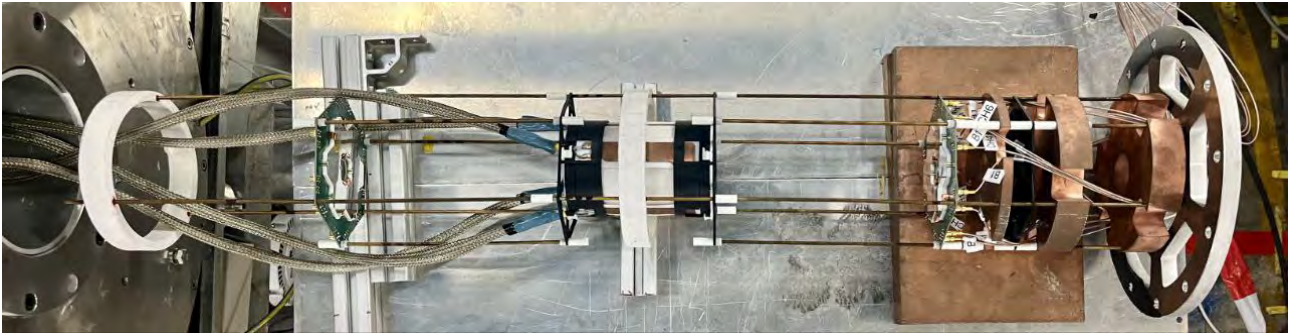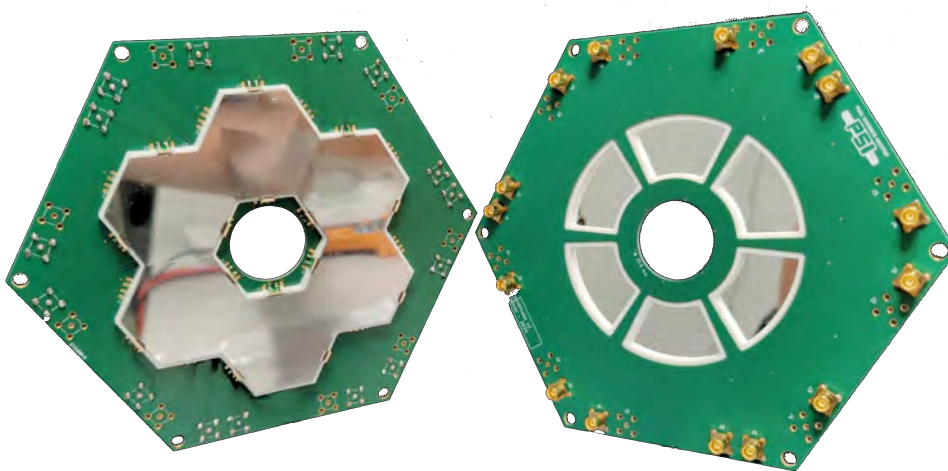entum of $150\,\text{MeV}/c$ then passed through an entrance detector and a veto before being stopped in a plastic target in the center of the magnet. The size of the target was chosen such that decay muons were also stopped within the target. The decay positrons, being minimally ionizing particles reach the detectors without significant energy loss. The asymmetry between the upstream and downstream detectors was measured as a function of the time relative to the last magnetic pulse, allowing the study of detection related systematic effects.

During the test beamtime we recorded about 2×10^7 triggers with 35 waveforms per trigger: the SiPMs of the two hexagonal detectors, veto detectors for anti-coincidence with pions from the beam, the HIPA RF signal for additional particle-ID from time-of-flight measurements, a signal proportional to the current in the kicker, and the trigger giving start of the kicker and acquisition.

Half of the waveforms were collected with current passing through the kicker coils and half without. We will use the waveforms without the kicker to establish the baseline of operation of the end-cap detectors. The efficiency with which the scintillation tiles detect decay positrons is determined for scintillator tiles equipped with three SiPMs. The ratio between the rate of triple coincidences T (all 3 SiPMs register a signal) to the rate of double coincidences D (any 2 SiPMs register a signal) is proportional to the detection efficiency.

This parameter T/D will also be calculated for the events detected after a kick has been issued. We will analyze the relationship between the detection efficiency and time to the previous kicker signal. Recording the full waveforms allows us to design mitigation strategies and digital filters that can then be transferred to the final detector design and implemented in hardware or software.

During this beam time the detectors were exposed to similar levels of radiation as for the entire duration the Phase I experiment. We will analyze the data to look for signs of degradation of the SiPMs with received dose, which is a critical input for the design of the final Phase I scintillation tracker.
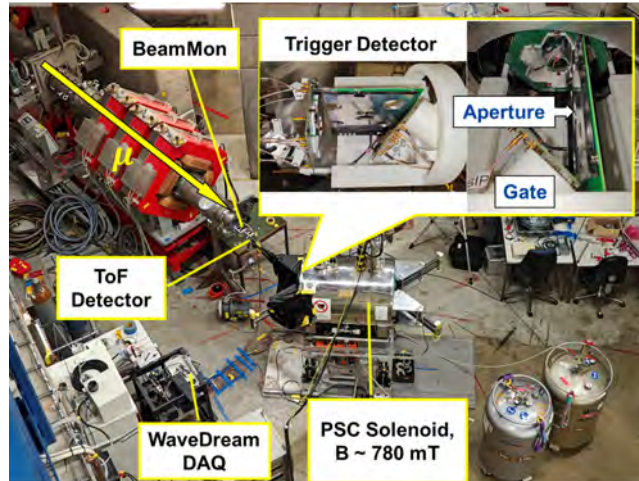
Figure 44: Set-up of the $\pi E1$ test beam October 2024. Inset shows the upgraded prototype of the trigger detector, comprised of a gate scintillator and the aperture scintillator.
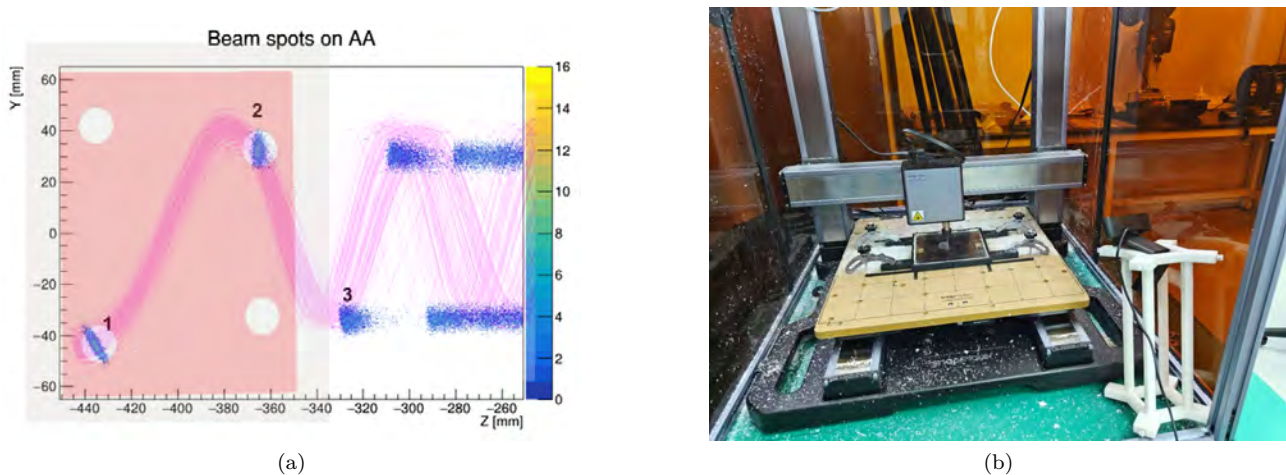

(a)

(b)

Figure 45: a) Obtaining dimensions and geometry of Aperture with simulation, red overlay illustrating the Aperture scintillator; b) fabrication of Aperture openings with CNC cutting machine.

C.   piE1 - testing injection and trigger

In October 2024, an upgraded prototype of the muon trigger detector was tested at the $\pi E1$ beamline (Fig. 44). The upgrade is expected to perform the anti-coincidence scheme in a magnetic field, while also generating a fast TTL-signal to be used for triggering the magnetic pulse kick (see section on fast electronics). The telescope detector in the 2022 prototype was upgraded into an aperture scintillator (Fig. 44 inset) to accommodate beam trajectories in a magnetic field. Dimensions and geometry of the hole openings are obtained from Geant4-based simulation (Fig. 45a) and subsequently fabricated with a CNC cutting machine (Fig. 45b). Both, the gate and aperture are Eljen EJ-200 scintillators, readout by NDL EQ20-3030 SiPMs. The gate detector is read-out with four SiPMs, interfaced with a lightguide from Eljen. The aperture detector is read-out with 6 SiPMs connected in parallel. All SiPMs are light-coupled with BC-603 optical grease. An exit detector also of plastic scintillator and SiPMs was installed $\approx 20\,\text{mm}$ downstream of the aperture. Signal digitization of all SiPM channels was performed using the WaveDAQ system.

This test beam aimed on the characterization of the trigger detector by evaluating the following aspects: i) performance of fast electronics readout, ii) agreement of event topology between measurement and simulation, and iii) induced positron background by the aperture.

Two beam configurations were used to adapt to the test beam condition in air. A e^+ beam at $10\,\text{MeV}/c$ is expected to spiral through the aperture and reach the exit detector, demonstrating the anti-coincidence scheme with all aperture openings (Fig. 46a). The Trigger Detector was initially designed for muon detection and is thus expected to be less efficient under the e^+ beam configuration. To complement this, a beam configuration with μ^+ at $22.5\,\text{MeV}/c$ was also
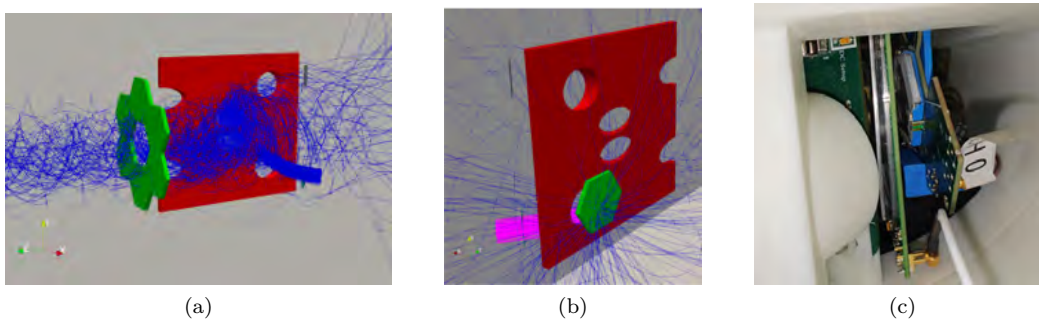
Figure 46: Visualisation of simulated events with a) 10 MeV/c e^+ reaching the full Exit Detector downstream of the Aperture; b) 22.5 MeV/c muons stopped at the lone Exit detector placed immediately behind the first Aperture opening; c) Placement of the lone Exit detector immediately behind the first Aperture opening.
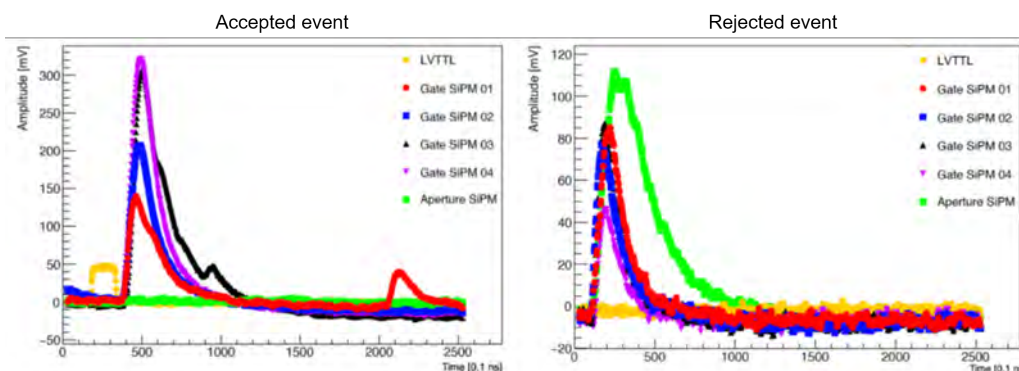

Figure 47: Left: typical waveform of an accepted event, signal present from all four Gate SiPMs and no signal from the Aperture SiPM along with the TTL signal produced; right: typical waveform of a rejected event.

used (Fig. 46b). In this beam configuration, the beam will only pass through the first hole of the aperture scintillator. The exit detector was re-positioned directly behind the first opening to record events that were not vetoed (Fig. 46c).

A total of about three million effective events were recorded, about one million for e^+ and ≈ 2 million for μ^+. The data were taken with five trigger patterns, i) trigger by anti-coincidence TTL signal, ii) trigger by gate, iii) trigger by aperture, iv) trigger by gate-aperture coincidence, v) trigger by aperture in anti-coincidence with gate. Each trigger pattern was recorded with beam injected clockwise (CW) and counter-clockwise (CCW).

Figure 47 shows typical waveform of *accepted* (Gate anti-coincidence with the Aperture) and *rejected* (Gate coincidence with the Aperture) events. A preliminary analysis was conducted to examine the fraction of accepted events. This is done by comparing the fraction accepted events from offline selection and the fraction of accepted events from TTL signal (fast electronics supposedly to produce TTL signal only for events satisfying the anti-coincidence scheme). The analysis utilized data sets from both the TTL signal trigger (T3) and the Gate trigger (T4). For the T3 data set, about 95% of events were accepted events under the e^+ beam configuration; about 100% of events were accepted events under the μ^+ beam configuration. As for the T4 data set, about 46% of events were accepted events under the e^+ beam configuration; about 77% of events were accepted events under the μ^+ beam configuration. Rejected events are currently being studied. In-depth analysis with the electronics effects accounted for is still on-going.

On the electronics side, one of the key quantities of interest is the propagation delay. It is defined as the time interval between the moment when all SiPM signals exceed the threshold (10 mV for e^+ and 15 mV for μ^+, approximately 4 mV per photon) and the half-height of the rising edge of the LVTTL trigger output. The propagation delay results for CW and CCW muons, as well as positrons, are presented in Fig.48, with an average value of 5.920 ± 0.482ns. The electronics exhibited stable performance under a magnetic field and during extended operation, as evidenced by consistent propagation delay measurements for CW/CCW μ^+ and e^+ recorded at various time points.

The anti-coincidence efficiency of the detector is defined as the ability of the electronics to output LVTTL trigger signals under anti-coincidence conditions. The anti-coincidence condition refers to a scenario where a particle hits the gate detector but not the aperture detector, in which case an LVTTL trigger signal is expected to be generated. For μ^+, the efficiency exceeds 99%, while for e^+, it is slightly lower at over 98%. This discrepancy arises from two main factors. First, the hysteresis of the discriminator requires the signal amplitude to exceed a threshold by approximately 2 mV for activation. For instance, with a 10 mV threshold, the discriminator is triggered only when the signal surpasses
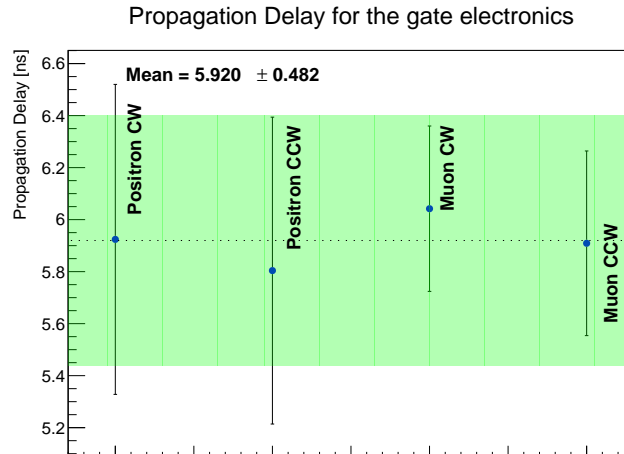
Figure 48: Propagation delay results for the Beam test 2024.

Table VI: Properties of the entrance detector prototype and PSI muEDM requirements.

	Electronics Board	muEDM requirements
Anti-Coincidence efficiency	99.5%	$\geqslant 95\%$
Coincidence efficiency	97.4%	$\geqslant 95\%$
Propagation delay [ns]	5.9 ± 0.5	$\leqslant 15$
Trigger Signal Voltage [V]	2.5	> 1.7
Trigger Signal Width [ns]	20.0 ± 6.0	> 3

12 mV, leading to a small fraction (<2%) of cases where signals exceed the threshold but fail to overcome the hysteresis, preventing trigger output. Second, the energy deposition in the gate detector is higher for μ^+ than for e^+, with average energy depositions of $\langle E_{\mu^+} \rangle = 0.272\, \mathrm{MeV}$ and $\langle E_{e^+} \rangle = 0.017\, \mathrm{MeV}$, respectively. This results in larger SiPM signal amplitudes for μ^+, making it easier to exceed the threshold and overcome the discriminator's hysteresis.

The coincidence efficiency is defined as the probability of the aperture detector suppressing LVTTL trigger signals under coincidence conditions. The coincidence condition refers to a scenario where a particle hits both the gate and aperture detectors, in which case no LVTTL trigger signal is expected to be produced. Among coincidence events, 97.38% successfully prevented LVTTL trigger output, while 2.62% produced unexpected LVTTL signals. Although these signals could activate the pulsed magnetic field, no muons are ejected as they are stopped within the aperture scintillator, resulting in empty events recorded by the data acquisition system. The failure of coincidence suppression in LVTTL signal production is primarily due to the large capacitance introduced by the parallel connection of six SiPMs in the aperture detector. This increases the signal rise time, causing the time window of the aperture trigger signal to not fully overlap with that of the gate trigger signal, resulting in the output of a narrow LVTTL trigger.

The properties of the electronics, summarized in Tab. VI, meet the requirements of the PSI muEDM experiment. Future efforts will focus on further optimizations, such as refining the wiring of the aperture SiPMs and adjusting the connections and cable lengths between the gate and aperture detectors. These improvements aim to enhance performance and provide a solid foundation for the upcoming beam test in 2025.

V. PLANNING AND SCHEDULE

A. Organizational structure

The collaboration plans to sign its "Framework collaboration agreement" (MoU in Fig. 49) between all participating institutions in April 2025. During the autumn collaboration board meeting in November 2024, Angela Papa and Philipp Schmidt-Wellenburg were elected as co-spokespersons. Figure 49 displays the organizational chart of the collaboration top level.

The principal governing body is the "collaboration board" (CB) consisting of a representative of each collaboration member. It nominates and elects two co-spokespersons, at least one of them from PSI, managing the collaboration on a
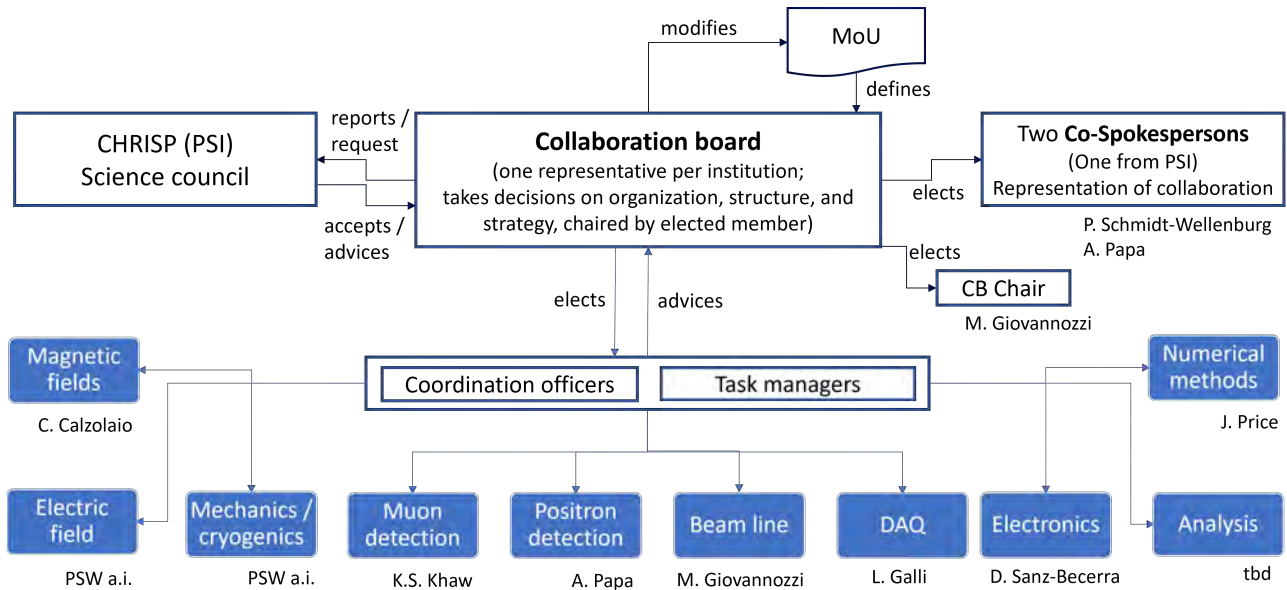
Figure 49: Organigram of the muEDM collaboration. All offices, except the two Co-spokespersonships, are optional and will be elected on request of the board.

day-to-day basis, and representing it externally. The board proposes and reports its research program and progress to PSI's CHRISP research committee, and other governing bodies on demand. In addition, it designates all additionally required offices, e.g. technical coordinator, CB-chair, and task managers responsible for the implementation of the research and development strategy defined by the board.

B. Tasks and planning phase 1

The proposed project, to set up and commission an apparatus to demonstrate the frozen-spin technique and search for a muon EDM with unprecedented sensitivity, is organized into a number of tasks. Figure 50 shows a simplified GANTT chart of the Phase I experiment. A full interdepedet planning is realized using MICROSOFT PROGRAM MANAGER to assure a full overview of all task and the identification of the critical path. The milestones of the single most critical task, the procurement of a fastm triggered pulse generator are noted alphabetically, while the milestones of the overall project are numerated.

The status of the listed tasks is indicated by three symbols: □ not started, ⊡ on the way, ⊠ finished.

Magnetic field The magnetic field is tightly connected to the injection and storage of muons inside the solenoid. The task covers all aspects of the magnetic field:

- ⊠ magnetic-field mapping of the two existing solenoid magnets at PSI,
- ⊠ calculation and optimization of field correction and weakly-focusing coil (WFC) to adjust the magnetic field for best performance,
- ⊠ design of correction and weakly-focusing coil,
- ⊡ design of the pulsed field coil,
- ⊡ design and construction of a fast compact optical magnetometer to measure the pulsed magnetic field and eddy currents,
- ⊡ construction of all coils,
- ⊡ specification, design, procurement of the pulse power supply,
- ⊡ specification and procurement of current power supplies for WFC and correction coils,
- ⊡ assembly, test, and characterization of pulse coil,
- □ assembly and test of weakly-focusing and correction coil,
- □ measurement of the magnetic field including all coils.

Electric field The electric field is required to establish the frozen-spin condition and can be used to tune the $(g-2)$-frequency to measure the magnetic field and potential systematic effects. The task covers all aspects of the electric field:

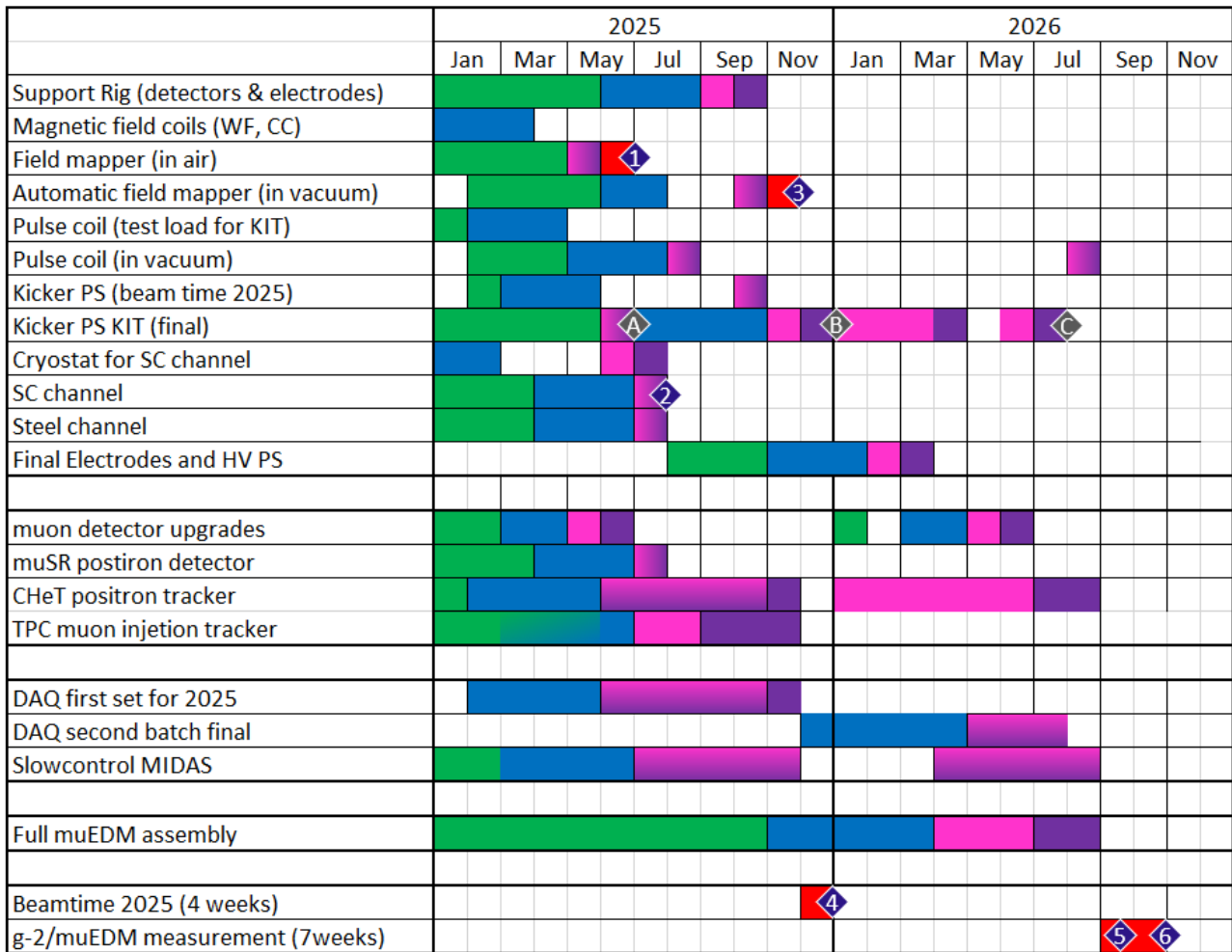| Task	2025 Jan	Mar	May	Jul	Sep	Nov	2026 Jan	Mar	May	Jul	Sep	Nov
Support Rig (detectors & electrodes)												
Magnetic field coils (WF, CC)												
Field mapper (in air)			①									
Automatic field mapper (in vacuum)						③						
Pulse coil (test load for KIT)												
Pulse coil (in vacuum)												
Kicker PS (beam time 2025)												
Kicker PS KIT (final)			Ⓐ			Ⓑ				Ⓒ		
Cryostat for SC channel												
SC channel				②								
Steel channel												
Final Electrodes and HV PS												
muon detector upgrades												
muSR postiron detector												
CHeT positron tracker												
TPC muon injetion tracker												
DAQ first set for 2025												
DAQ second batch final												
Slowcontrol MIDAS												
Full muEDM assembly												
Beamtime 2025 (4 weeks)						④						
g-2/muEDM measurement (7weeks)											⑤ ⑥	

Figure 50: Schedule of top level tasks and milestones. (M1) Confirmation of optimized magnetic field, (M2) demonstration of SC shielding, (M3) field map of the magnetic field in vacuum including SC channel, (M4) tracking of muon injection, muSR measuremet of the intial phase, stopping of muons in the weakly focusing field, and demonstration of the CHeT performance, (M5) adjust electric field by tuning $(g-2)$-precession to zero, and (M6) data-taking in muon EDM mode. (A) Stage modules are designed, produced and performance validated, (B) generatore design finalized, ready for production, (C) Working generator, knowledge transfer to PSI, complete documentation.

- ☐ design and test prototypes of electrodes,
- ☒ specification, design, procurement of the high-voltage power supply,
- ☐ design and manufacture electrode,
- ☐ specification, procurement, and tests of vacuum feed through.

Mechanics and cryogenics The superconducting injection channel needs to be cooled to about 4.2 K, further it needs to be heated to above the critical temperature, each time the main SC magnet is ramped. To change from clockwise to counterclockwise injection, the SC magnet has to be moved vertically by about 90 mm. The coils, electrodes and detectors need to be mounted on a support structure within the solenoid. The task covers:

- ☒ Procurement of cryocooler with 1 W cooling power at 4.2 K
- ☐ thermometry and temperature control for SC shield and heat screens,
- ☐ design, procurement, and assembly of the cryostat,
- ☐ mounting structures for inside solenoid bore,
- ☒ experimental support structure adjustable in height for CW and CCW injection,
- ☐ setup and maintenance of a CAD model of the experiment.

Muon detection At several positions along the muon injection trajectory, we will use scintillating detectors for detection and monitoring. The task covers all muon detectors:

  ⊠ segmented muon entrance monitor for beam steering and monitoring of the incident flux;

  ⊠ ToF detector at the entrance of the injection channel

  ⊡ entrance trigger detector at the exit of the injection channel,

  ⊡ scintillating apertures to generate a trigger in anti-coincidence with the entrance detector, when a muon is within the acceptance phase space for storage,

  ⊡ end-detector to detect muons which cannot be stored and pass the central region of the solenoid,

  ⊡ auxiliary scintillating detectors for beam diagnostics.

Positron detection All information on muon spin precession is imprinted on kinematics of the ejected positron when the muon decays. The task covers all detectors to reconstruct positron tracks from decay:

  ⊡ Design, procurement, and assembly of muSR detectors to measure the initial phase of the muon spin as a function of spin-rotator settings.

  ⊡ Design and simulation of position sensitive positron detector suitable to measure the $g-2$ precession frequency as function of the electric field and the EDM signal, the change of the longitudinal asymmetry in the frozen-spin state, based on multiple layers of scintillating fibers.

DAQ and electronics The DAQ and electronics task takes care that in each experimental step, demonstrating the ability to deploy the frozen-spin technique for a measurement of the muon EDM, all relevant data are correctly acquired and electronics meet PSI's laboratory standards of safety. The task covers:

  ⊠ Decision on DAQ system

  ⊠ Procurement and implementation of WaveDAQ for muon beam monitor.

  ⊡ Procurement of FERS modules DAQ for all detectors except muon beam monitor and implementation in MIDAS.

  ⊡ electronics to measure magnetic fields,

  ⊡ electronics to control the high voltage supply,

  ⊡ electronics to measure temperatures and control the cryostat,

  ☐ connection and interface to the beam line control system,

  ⊡ and safe storage of all data in open data fit storage facilities.

Beam line The secondary beam line πE1 serves many different experiments every year, possibly with very different requirements. This task comprises the optimization of the beam line for an injection into the experiments injection channel:

  ⊡ Optimization of transverse phase space and flux, and minimization of the momentum bite for the existing beam line;

  ⊠ Measurement of transverse phase space and flux of muE1 in Z-configuration

  ⊡ Optimization of transverse phase space and flux, and minimization of the momentum bite for the Z-configuration of muE1.

  ☐ investigation, and design of nonlinear beam elements to adjust beam phase space to acceptance phase space.

Analysis and Simulations The analysis and simulation task encompasses a start-to-stop simulation of the experiment and the preparation of the analysis based on synthesized simulation data. The task covers:

  ☐ beam line simulation and transport calculations from proton target to exit of secondary beam line

  ⊡ injection and storage simulations using Monte Carlo methods and surrogate models for design and parameter optimization,

  ⊡ simulation of detector response using Monte Carlo methods to synthesize toy data to develop an automated and blinded analysis

  ☐ an automated and blinded analysis for the final data demonstrating the frozen-spin technique and searching for an EDM.

C. Long-term perspective including Phase-II

Already during Phase-I certain aspects of the Phase-II instrument will be studied using finite element methods, Monte Carlo physics simulations, and machine learning algorithms for optimization. Together with the gradual progress of Phase-I, we will converge to an instrument design by the end of 2027. The second phase instrument coupled to a muon beam with $p \geq 125\,\mathrm{Mev/c}$ will further increase the sensitivity by a factor 50.

VI.   REQUEST FOR BEAM AND TECHNICAL SUPPORT

A.   Beam time request - 2025

In 2025 we would like to request a four-week beam time at piE1 to demonstrate crucial steps for a first successful muEDM measurement in 2026. We note for each item the measurement duration and expected setup time as (x days + y days).

Muon injection and muon tracking (4.5 days + 3.5 days) using a dedicated auxiliary gaseous time projection chamber (TPC)[22], to image the spiral injection in the space where the muon trigger detector will be placed. After a successful imaging, we will remove the TPC, mount the muon trigger, and measure the coincidence between the trigger signal and the muon end detector as a function of correction coil currents. By maximizing the coincidence rate we demonstrate a successful off-axis injection/

muSR initial phase measurement (4 days+2 days) . Once the injection is optimized, we will mount a thin copper foil in the center of the solenoid field, $z = 0$. Muons entering will now be stopped at the center and precess until they decay. By recording the decay asymmetry, left/right and top/bottom, with a set of simple scintillating detectors we record the muSR frequency and can deduce the mean initial phase of the muon spin.

Muon storage (4.5 days+1.5 day) . After the removal of the copper foil and mounting of the pulse coil and weakly focusing coil, we will measure the storage efficiency using the modified pulse generator already deployed in the 2024 beam time. By systematically changing the pulse strength and possibly the strength of the weakly focusing field, we will try to minimize the rate of coincidence between entrance trigger and end detector. A sign for successful muon storage.

Positron detection using CHeT (4 days+4 days) In the last stage we will mount the first few elements of the CHeT detector. We will then repeat the storage experiment while observing the positron detection rate in the CHeT. If time permits we would then try to measure for the first time in this setup the (g-2) precession.

Our planning for 2025 and 2026, taking possible contingencies due to delays in manufacturing or procurement into account is outlined in Fig. 50.

1.   Demonstration of spiral injection into a 2.5 T *solenoid field, measurement of the initial spin phase of the muon, and storage of muons in a weakly-focusing field using muons from piE1*

a.   Spiral injection

The spiral injection into the solenoid at 2.5 T is an essential milestone the collaboration wants to demonstrate in 2024. For this purpose several essential parts of the final experiment need to work.

Cryostat The superconducting shield, either made of sheets of NbTi low temperature superconductors or ReBCO tape wound onto a tube need to be cooled well below their transition temperatures, 10 K and 90 K respectively. For this purpose we have acquired a Sumitomo GM cooler with 1 W cooling power at 4.2 K on the second stage to which the shields will be connected. The superconducting shields will be surrounded with a 50 K-shield to reduce radiative heating. All parts are in production and delivery is expected for the third week of February.

Superconducting shield The last 400 mm of the injection channel need to be shielded by a superconducting shield, see Section II F. The superconducting material will be inside two copper half shells cooled by the a braided flexible connection to the second stage of the cryo cooler. The assembled low temperature injection channel will be mounted inside the 50 K shield with ceramic support to reduce heat conduction while taking up the magnetic forces and transferring them to the shield.

muon TPC The muon TPC (See sec. II I) will be mounted at the upstream end of the holder system, it will be inserted into the magnet bore and its precise position will be measured with an optical survey. Muons will be tracked, possibly with both CW and CCW injections. We will verify the consistency of the muon trajectories with the expectations and the symmetry of the two injection modes.

Entrance detector Right after the exit of the injection channel we will mount one of the existing thin scintillating detectors, already used in the 2024 beam time, to detect all muons entering the strong magnetic field region inside the bore.

Correction coil For an efficient spiral injection, the magnetic field of the solenoid has to be modified using two coils positioned at $z = \pm 250$ mm with respect to the center of the solenoid. We require a current density of $0.7 \, \text{mm}^2$, giving us a safety factor of two. We will deploy a conventional coil, wound from copper wire AWG12, with 180 turns. This will result in a maximum heat dissipation of several Watts which will be cooled using a single turn water heat exchanger.

Exit detector We will use the same scintillating detector as shown in Fig. 43 to detect muons which pass through the solenoid bore after injection. By measuring the coincidence rate between entrance detector and exit detector, we will optimize the correction coil current for the best spiral injection.
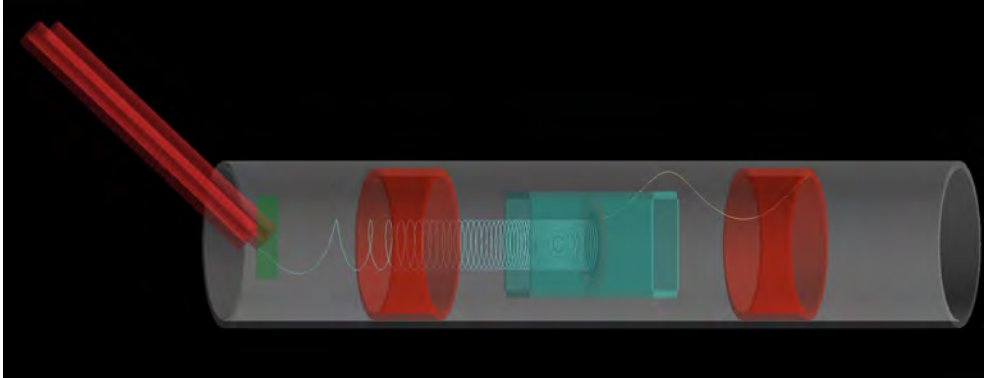
Figure 51: Image of a G4Beamline simulation. A muon enters the solenoid through the injection channel, triggers the entrance detector and spirals into the central region. Here it is stopped in a 1 mm copper foil. The decay positron is detected using thick scintillators surrounding the target. By taking the asymmetry of opposing positron counters versus time we can measure the muon spin rotation and determine the initial spin phase.

b.   Measurement of ToF and the initial phase of injected muons

We plan to inject muons clockwise and counterclockwise, reversing the magnetic field and changing the injection channel by a vertical movement of the entire experiment, to cancel systematic effects arising from an imperfectly aligned electric field. For details see Ref. [15]. The cancellation only works for identical initial conditions of the muon, which in this case means momentum and spin. By measuring the time of flight through the injection channel for each muon individually, we can select identical momentum distributions in the analysis. Hence, the remaining uncertainty is the initial spin phase of the stored muons. This we will characterize by stopping muons in a thin target, e.g., a thin copper disc, in the center of the solenoid and measure the muon spin rotation signal with surrounding scintillating detectors.

This measurement requires the following components

ToF detectors The time of flight of each injected muon will be measured by using two thin scintillating detectors. One at the entrance of the injection channel, the other at its exit. The detectors exist and showed reliable performance in the 2023 test beam time.

Muon injection trigger The muon injection trigger will produce a TTL signal using the anti-coincidence between the ToF exit detector and a scintillating detector with openings along the nominal injection trajectory. This TTL signal can be used as start time for the muon spin rotation measurement. We will use the existing system from the 2024 test beam.

Positron detectors A minimum of four positron detectors made of thick scintillators will record the decay positrons as a function of time. The change in asymmetry between left and right, and up and down detectors, can be fitted with a decaying sinus giving access to the initial spin phase in the x-y plane of the solenoid.

DAQ A dedicated data acquisition system will be prepared to record the muon spin rotation signal as a function of time and muon time of flight. We plan to evaluate the CAEN FERS A5202 as a channel-by-channel scaler together with charge and time measurements. During the beam time, our objective is to assess the performance in terms of detector noise levels and resolution when interfaced with the FERS. Additionally, we aim to measure the limitations of the data acquisition (DAQ) rate associated with this technology. The results obtained during the beam time will help determine whether this DAQ system is suitable for adoption in the precursor experiment.

c.   Demonstration of muon storage in weakly focusing field

Once we have shown that muons pass through the injection channel and the solenoid bore, the next step will be to trigger the magnetic kick and store muons inside the solenoid. For this demonstration the following parts in addition to the elements discussed above will need to work.

Weakly-focusing coil Muons can be stored if the magnetic field in the center of the solenoid provides a weakly-focusing magnetic field gradient. This will be accomplished by a dedicated coil located at the center of the solenoid with an inner radius of about $r_{\mathrm{WFC}} \approx 50\,\mathrm{mm}$.

Magnetic pulse The short magnetic pulse, described in Sec. II H, required to kick the muons onto a stable orbit for storage, will be generated by the same coil and a modified power supply as the ones that were used piM1 beam time in 2024, see Sec. **??**.

We will measure the muon coincidence rate between the entrance and exit trigger as a function of delay time between trigger and pulse and as a function of the integral pulse power, adjustable via the voltage of the kicker power supply. In the case of successful storage, we expect a decline in count rate in the muon exit detector and an increase in counts in the central positron detector.

d. Test of CHeT positron tracker The last week of the beam time we will investigate the first cylindrical units of the CHeT detector. These tests using the full FERS DAQ system are crucial to identify shortcomings for the full detection scheme to measure the (g-2) precession frequency as function of the applied electric field and demonstrate the frozen-spin technique in 2026.

In total we ask for four weeks of beamtime. The first week will depoly the TPC injection tracker and demonstrate the spiral injection into the solenoid. The second week will be used to stop muons on a central copper foil to measure the initial spin phase to limit potential systematic effects. The third week will be used to demonstrate the storage of muons in the weakly-focusing field while the fourth week will test and investigate the CHeT scintillating fiber positron tracker.

VII.   ACKNOWLEDGMENTS

[1] K. Deb, A. Pratap, S. Agarwal, and T. Meyarivan. 'A fast and elitist multiobjective genetic algorithm: NSGA-II.' IEEE Transactions on Evolutionary Computation, 6(2002) 182. URL `http://dx.doi.org/10.1109/4235.996017`.

[2] S. S. e. a. H. Ma, Y. Zhang. 'A comprehensive survey on NSGA-II for multi-objective optimization and applications.' Artif Intell Rev 56, (2023) 15217. URL `http://dx.doi.org/https://doi.org/10.1007/s10462-023-10526-z`.

[3] I. M. Sobol. 'On the distribution of points in a cube and the approximate evaluation of integrals.' U.S.S.R. Computational Mathematics and Mathematical Physics, 7(1967) 86.

[4] J. Feinberg and H. P. Langtangen. 'Chaospy: An open source tool for designing methods of uncertainty quantification.' Journal of Computational Science, 11(2015) 46. URL `https://doi.org/10.1016/j.jocs.2015.08.008`.

[5] 'G4Beamline.' URL `https://www.muonsinc.com/Website1/G4beamline`. Muons Inc.

[6] A. Holmberg. 'Optimization of the Muon Injection for a Muon EDM Experiment.' Tech. rep., ETH Zurich (2021).

[7] A. Paszke *et al.* 'PyTorch: An Imperative Style, High-Performance Deep Learning Library.' Proceedings of the 33rd International Conference on Neural Information Processing Systems (2019) 1912.01703.

[8] D. P. Kingma and J. Ba. 'Adam: A Method for Stochastic Optimization.' CoRR, abs/1412.6980(2014). URL `https://api.semanticscholar.org/CorpusID:6628106`.

[9] A. L. Maas. 'Rectifier Nonlinearities Improve Neural Network Acoustic Models.' Proceedings of the 30th International Conference on Machine Learning, Vol. 28, 3. (2013) URL `https://api.semanticscholar.org/CorpusID:16489696`.

[10] K. Developers. 'Callbacks-Keras Documentation.' (2019).

[11] Geuzaine, Christophe and Remacle, Jean-Francois. 'Gmsh.' URL `http://http://gmsh.info/`.

[12] C. Geuzaine. 'GetDP: a general finite-element solver for the de Rham complex.' PAMM Volume 7 Issue 1. Special Issue: Sixth International Congress on Industrial Applied Mathematics (ICIAM07) and GAMM Annual Meeting, Zürich 2007, vol. 7. Wiley (2008) 1010603–1010604.

[13] T. Roberts and D. Kaplan. 'G4beamline simulation program for matter-dominated beamlines.' (2007) 3468 − 3470. URL `http://dx.doi.org/10.1109/PAC.2007.4440461`.

[14] D. Barna, M. Novák, K. Brunner, *et al.* 'NbTi/Nb/Cu multilayer shield for the superconducting shield (SuShi) septum.' IEEE Trans. Appl. Supercond., 29(2018) 4900108. URL `http://dx.doi.org/10.1109/TASC.2018.2872860`. 1809.04330.

[15] G. Cavoto, R. Chakraborty, A. Doinaki, *et al.* 'Anomalous spin precession systematic effects in the search for a muon EDM using the frozen-spin technique.' (2023). 2311.10508.

[16] X. Llopart, R. Ballabriga, M. Campbell, *et al.* 'Timepix, a 65k programmable pixel readout chip for arrival time, energy and/or photon counting measurements.' Nucl. Instr. Meth. Phys. Res. A, 581(2007) 485. URL `http://dx.doi.org/10.1016/j.nima.2007.08.079`.

[17] G. Cavoto *et al.* 'Operating the GridPix detector with helium-isobutane gas mixtures for a high-precision, low-mass Time Projection Chamber.' JINST, 18(2023) P10035. URL `http://dx.doi.org/10.1088/1748-0221/18/10/P10035`. 2305.03599.

[18] A. Adelmann, A. Bainbridge, I. Bailey, *et al.* 'A compact frozen-spin trap for the search for the electric dipole moment of the muon.' submitted to EPJC, (2025).

[19] M. Sakurai. Towards a Search for the Muon Electric Dipole Moment using the Frozen-Spin Technique. Ph.D. thesis, ETH Zürich (2022). DISS. ETH NO. 28992.

[20] E. Prat and M. Aiba. 'Four-dimensional transverse beam matrix measurement using the multiple-quadrupole scan technique.' Physical Review Special Topics-Accelerators and Beams, 17(2014) 052801.

[21] M. Chung, H. Qin, and R. C. Davidson. 'Twiss parameters and beam matrix formulation of generalized Courant–Snyder theory for coupled transverse beam dynamics.' Physics of plasmas, 17(2010).

[22] M. Giovannozzi, M. Hoferichter, G. Hiller, *et al.* 'Status report 2023 of the search for a muon electric dipole moment.' internal PSI report, (2025).